ABSTRACT

Title of dissertation: Strategies for Coupling Global and Limited-Area Ensemble Kalman Filter Assimilation

Dagmar Merkova, Doctor of Philosophy, 2011

Dissertation directed by: Istvan Szunyogh and Eugenia Kalnay
Department of Atmospheric and Oceanic Science

This thesis compares the forecast performance of four strategies for coupling global and limited area data assimilation: three strategies propagate information from the global to the limited area process, while the fourth strategy feeds back information from the limited area to the global process. All four strategies are formulated in the Local Ensemble Transform Kalman Filter (LETKF) framework.

Numerical experiments are carried out with the model component of the National Centers for Environmental Prediction (NCEP) Global Forecast System (GFS) and the NCEP Regional Spectral Model (RSM). The limited area domain is an extended North-America region that includes part of the north-east Pacific. The GFS is integrated at horizontal resolution T62 (about 150 km in the middle latitudes), while the RSM is integrated at horizontal resolution 48 km. Experiments are carried out both under the perfect model hypothesis and in a realistic setting. The coupling strategies are evaluated by comparing their deterministic forecast performance at 12-hr and 48-hr lead times.

The results suggest that the limited area data assimilation system has the potential to enhance the forecasts at 12-hr lead time in the limited area domain at the synoptic and sub-synoptic scales (in the global wave number range of about 10 to 40). There is a clear indication that between the forecast performance of the different coupling strategies those that cycle the limited area assimilation process produce the most accurate forecasts. In the realistic setting, at 12-hr forecast time the limited area systems produce more modest improvements compared to the global system than under the perfect model hypothesis, and at 48-hr forecast time the global forecasts are more accurate than the limited area forecasts.

Strategies for Coupling Global and Limited-Area Ensemble Kalman Filter Assimilation

by

Dagmar Merkova

Dissertation submitted to the Faculty of the Graduate School of the
University of Maryland, College Park in partial fulfillment
of the requirements for the degree of
Doctor of Philosophy
2011

Advisory Committee:
Professor E. Kalnay, Chair
Associate Professor Istvan Szunyogh (Texas A&M University, Advisor)
Professor Edward Ott, Dean's representative
Professor J. Carton
Professor Kayo Ide

Acknowledgments

It is my pleasure to thank the many people who made this thesis possible. First, I would like to express my deepest gratitude to my supervisor, Istvan Szunyogh. I'm grateful to him for the endless support and patience during all these years. Without his guidance and persistence this thesis would not have been possible.

I'm thankful to all the professors and students of the Weather-Chaos group at UMD for the many fruitful discussions that we had. It was an honor to be a part of such a group. I would especially like to express my gratitude to Eugenia Kalnay for her professional advice, kind words and encouragement thst she offered me all these years. She gave me strength to overcome difficult times, and was a great example to me. I would also like to thank Professor Edward Ott, who offered me invaluable assistance and guidance and helped me to continue in my research for many years. I'm grateful to Gyorgyi Gyarmati for her help with observations, and to Eric Kostelich for sharing his LETKF code and for challenging my knowledge of FORTRAN. I would like to thank Henry Juang for his advice in implementing the NCEP RSM on the local system. I want to thank James Carton and Kayo Ide for their time, valuable advice and encouragement.

Many thanks to David Kuhl for the hours of discussions and listening, and to Elizabeth Satterfield for endless conversations (not only about GRADS) on our rollerblade lunchbreaks. I also thank Emily Becker for sharing her English language skills by patiently proofreading and listening to my talks and assignments during my studies.

Lastly, and most importantly, I'm deeply indebted to my daughter for her unconditional love. I can never turn back the clock and give her the time that I spent on my research instead, but I will always be there for her as she has been for me.

Table of Contents

List of Figures

List of Abbreviations

GFS	Global Forecast System
LETKF	Local Ensamble Transform Kalman Filter
NCEP	National Center for Enviromental Prediction
RSM	Regional Spectral Model
UTC	Universal Time Coordinated

Chapter 1

Introduction

A state-of-the-art atmospheric limited area model uses time-dependent lateral boundary conditions provided by a global atmospheric model. In current practice, the initial conditions for the limited area model are either analyses prepared using the global model and interpolated to the higher resolution grid of the limited area model, or analyses prepared by using a data assimilation system specifically designed to produce initial states for use by the limited area model. In the latter case, the analysis inside the limited area domain is obtained independently of the global analysis (e.g., Torn et al. 2006; Zhang et al. 2006; Huang et al. 2009). The aforementioned two approaches are motivated by the practical constraint that most weather prediction centers and research groups who run limited area models have access to global analysis products, but do not have the capability to produce global analyses. The only exceptions are a handful of operational NWP centers, e.g., the National Centers for Environmental Prediction (NCEP), who prepare both global and limited area analyses, but, mainly for practical reasons, follow one of the two aforementioned approaches.

In this thesis, we consider the scenario in which we have access to both the global and the limited-area model and a model-independent data assimilation system. Our goal is to begin to address the problem of finding the configuration of

the coupling between these three components of the forecast system, which provides the best global and limited area model forecasts. In particular, we compare the forecast performance of the system for different coupling strategies using both simulated and operationally used observations of the atmosphere. In our experiments, the global model is the model component of the Global Forecast System (GFS) of the National Centers for Environmental Prediction (NCEP) (Sela 1980) integrated at a T62L28 (about 150 km) horizontal resolution, the limited area model is the Regional Spectral Model (RSM) of NCEP (Juang 1992; Juang and Kanamitsu 1994; Juang et al. 1997; Juang and Hong 2001) integrated at 48 km and L28 resolution, while the data assimilation system is the Local Ensemble Transform Kalman Filter (Ott et al. 2004; Hunt et al. 2007; Szunyogh et al. 2008). We choose the NCEP RSM for this study because along with the NCEP GFS model it has the most consistent dynamics among all limited area models. In particular, the two models share the same physical parametrization packages and the GFS model solution affects the RSM solutions not only at the lateral boundaries, but also in the entire limited area domain. Using these two particular models in a coupled system minimizes the chance of spurious transient behavior that may be introduced when information is propagated from one model to the other. In addition, this configuration allows for a clean comparison in which two models of similar quality are used. If the two models were of significantly different quality, it would not be possible to separate the effects of having higher resolution model information in the limited area from the effects of having model dynamics or physics of a different quality in the limited area. We design numerical experiments to start assessing the forecast value added

by the limited area assimilation.

The structure of the thesis is as follows. Chapter 2 presents our theoretical considerations for the coupling strategies. In particular, we describe the relationship between the coarse resolution global fields and the higher resolution limited area fields for an ensemble transform data assimilation scheme. Chapter 3 describes the components of the coupled global/limited area analysis-forecast system we use in our numerical experiments. Chapter 4 summarizes our results and findings for both the perfect and imperfect model scenarios.

Chapter 2

Data Assimilation

To design strategies for the coupling of a global and a limited area data assimilation system, we assume that the higher resolution limited area model provides a more accurate representation of the atmospheric dynamics in the limited area than does the global model. Our goal is to take advantage of the availability of this presumed better model information within the limited area to improve the quality of the analyses. We introduce our strategies assuming that the data assimilation component is based on an ensemble transform algorithm (e.g., Bishop et al. 2001; Hunt et al. 2007). While Strategy 1 (interpolation of low resolution analysis) is a conventional approach, which could be easily implemented using any data assimilation algorithm, and Strategy 2 and 3 (noncycled and cycled regional analysis) could be implemented using any ensemble-based scheme, Strategy 4 (analysis with feedback) takes advantage of the fact that the ensemble transform algorithm provides a straightforward way to propagate information from the limited area data assimilation process to the global process.

2.1 Global and limited area model dynamics

The global model dynamics $\mathbf{g}$, defined by

$$\mathbf{x}_g(t_f) = \mathbf{g}[\mathbf{x}_g(t_i)], \tag{2.1}$$

propagates an estimate $\mathbf{x}_g(t)$ of the global atmospheric state between an initial time t_i and a final time t_f. The components of $\mathbf{x}_g(t)$ are the spatially discretized atmospheric state variables (e.g., temperature, components of the wind vector, surface pressure, humidity variables). The limited area model dynamics $\mathbf{f}$, defined by

$$\mathbf{x}_l(t_f) = \mathbf{f}[\mathbf{x}_l(t_i), \mathbf{x}_g(t_i), \mathbf{x}_g(t_f)], \tag{2.2}$$

propagates an estimate $\mathbf{x}_l(t)$ of the atmospheric state in a limited area sub-domain of the globe at a resolution that is higher than that of $\mathbf{x}_g(t)$. We introduce the notation

$$\mathbf{x}'_l(t) = \mathbf{x}_l(t) - \mathcal{L}[\mathbf{x}_g(t)] \tag{2.3}$$

for the difference between the high resolution and the global state estimate in the limited area domain. In Eq. 2.3, $\mathcal{L}$ is the mapping from the state space of the global model onto the state space of the limited area model. In practice, this mapping is an interpolation from the lower resolution grid of the global model to the higher resolution grid of the regional model. While the limited area model resolves motions at scales that are smaller than the smallest scales resolved by the global model, there are scales that contribute to both $\mathbf{x}_l(t)$ and $\mathbf{x}_g(t)$. Thus, $\mathbf{x}'_l(t)$ cannot be simply considered to be a small scale perturbation to the global state vector in the limited area domain.

2.2 The motivation for coupled data assimilation

The derivation of the version of the LETKF which is considered in this study is based on the assumption that a model can provide a perfect representation of the dynamics of the observed system (Ott et al. 2004; Hunt et al. 2007). An implementation of the scheme on a numerical weather prediction model inevitably violates this assumption. One particular source of the error is the spatial discretization of the dynamics: the atmospheric state at time t is represented by a spatially continuous vector field $\mathbf{u}(t)$, while a model uses a finite-dimensional discretization $\mathbf{x}(t)$ of $\mathbf{u}(t)$ assuming that a suitable projection $\mathcal{P}$: $\mathbf{x}^t(t) = \mathcal{P}[\mathbf{u}]$ exists. (Here, the superscript t indicates that $\mathbf{x}^t(t)$ is the model state representation of the true atmospheric state.) Thus the finite-dimensional model dynamics $\mathbf{g}$ and $\mathbf{f}$ ignore an infinite number of interactions associated with the unresolved flow components. While parametrization of the sub-grid (unresolved) processes are designed to account for the effects of the unresolved scales on the resolved scale (e.g., Kalnay 2002), in general, a higher resolution model is expected to provide a more accurate representation of the atmospheric dynamics. The motivation for employing a limited area model is to provide a more accurate representation of the atmospheric dynamics in a limited area domain of particular interest. Our intended purpose in coupling the global and limited area data assimilation processes is to take advantage of the presumed superiority of the limited area model in the limited area domain to improve the accuracy of the limited area analyses.

2.3 Ensemble transform data assimilation schemes

An ensemble-based data assimilation system obtains the state estimate at analysis time t_n in two steps: (i) in the *forecast step*, a prior estimate of the state, called the background, and an estimate of the uncertainty in the background are obtained by propagating information from the previous analysis time t_{n-1} to $t_n = t_{n-1} + \Delta t$ using the model dynamics; and (ii) in the *state update step*, the prior estimates of the state and its uncertainty are updated based on the observations collected in the time window $[t_n - \Delta t/2, t_n + \Delta t/2]$.

Formally, the forecast step involves preparing a K-member ensemble of background forecasts $\{\mathbf{x}^{b(k)}(t_n),\ k = 1, \ldots, K\}$. For instance, in a global data assimilation system

$$\mathbf{x}_g^{b(k)}(t_n) = \mathbf{g}[\mathbf{x}_g^{a(k)}(t_{n-1})], \qquad k = 1, \ldots, K, \tag{2.4}$$

where $\{\mathbf{x}_g^{a(k)}(t_{n-1}),\ k = 1, \ldots, K\}$ are the members of the analysis ensemble at the previous analysis time t_{n-1}. The background state $\bar{\mathbf{x}}^b(t_n)$ is defined by the ensemble mean,

$$\bar{\mathbf{x}}^b(t_n) = K^{-1} \sum_{k=1}^{K} \mathbf{x}^{b(k)}(t_n), \tag{2.5}$$

while the uncertainty in the estimate $\bar{\mathbf{x}}^b(t_n)$ is described by the ensemble based estimate

$$\mathbf{P}^b(t_n) = (K-1)^{-1} \mathbf{X}^b(t_n)[\mathbf{X}^b(t_n)]^T, \tag{2.6}$$

of the background error covariance matrix. Here $\mathbf{X}^b(t_n)$ is the matrix whose k-th column is the k-th background ensemble perturbation $\mathbf{x}^{b(k)'}(t_n) = \mathbf{x}^{b(k)}(t_n) - \bar{\mathbf{x}}^b(t_n)$.

In an ensemble-transform-based data assimilation scheme (Ott et al. 2004; Hunt et al. 2007) the ensemble mean analysis is obtained by

$$\bar{\mathbf{x}}^a(t_n) = \bar{\mathbf{x}}^b(t_n) + \mathbf{X}^b(t_n)\mathbf{w}^a(t_n), \tag{2.7}$$

where the "weight vector" $\mathbf{w}^a(t_n)$ is the value of $\mathbf{w}$ that minimizes the quadratic cost function

$$J(\mathbf{w}) = (k-1)\mathbf{w}^T\mathbf{w} + (\mathbf{y}^o(t_n) - \mathbf{h}[\bar{\mathbf{x}}^b(t_n) + \mathbf{X}^b(t_n)\mathbf{w}])^T \mathbf{R}^{-1}(t_n)(\mathbf{y}^o(t_n) - \mathbf{h}[\bar{\mathbf{x}}^b(t_n) + \mathbf{X}^b(t_n)\mathbf{w}]). \tag{2.8}$$

Here, $\mathbf{y}^o(t_n)$ is the vector of observations assimilated at time t_n and the observation operator $\mathbf{h}(\mathbf{x})$ maps the model representation of the atmospheric state to observables at observation times. The observation operator is assumed to satisfy

$$\mathbf{y}^o(t_n) = \mathbf{h}[\mathbf{x}^t(t_n)] + \mathbf{e}(t_n), \tag{2.9}$$

where the vector of Gaussian random variable $\mathbf{e}(t_n)$ with mean $\mathbf{0}$ and covariance matrix $\mathbf{R}(t_n)$ represents the observation noise. In practice, $\mathbf{h}(\mathbf{x})$ is an interpolation of the model variables from the model grid points to the locations and times of the observations and a conversion of the model variables to the observed quantities.[1]

In addition to the analysis $\bar{\mathbf{x}}^a(t_n)$, an ensemble transform scheme also generates an ensemble of analysis perturbations by

$$\mathbf{X}^a(t_n) = \mathbf{X}^b(t_n)\mathbf{W}^a(t_n). \tag{2.10}$$

[1]Because the observations assimilated at time t_n are collected in the time window $t \in [t_n - \Delta t/2, t_n + \Delta t/2]$, the model is integrated for a time $\frac{3}{2}\Delta t$ from t_{n-1} to provide a background trajectory $\mathbf{x}^b(t)$ for the entire observation time window. The observation operator $\mathbf{h}$ operates on this background trajectory.

The analysis perturbations, which are the columns of $\mathbf{X}^a(t_n)$, are added to $\bar{\mathbf{x}}^a(t_n)$ to obtain the members of the analysis ensemble $\mathbf{x}^{a(k)}(t_n); k = 1, ..., K$. One approach to compute the weight vector $\mathbf{w}^a(t_n)$ and the weight matrix $\mathbf{W}^a(t_n)$ is through a square-root Kalman filter algorithm (e.g., Tippett et al. (2003)). The LETKF is a square-root filter (Ott et al. 2004; Hunt et al. 2007).

After the forecast step is completed, we use the background ensemble to define the ensemble of background observation vectors

$$\mathbf{y}^{b(i)} = \mathbf{h}(\mathbf{x}^{b(i)}), \tag{2.11}$$

their mean $\bar{\mathbf{y}}^b$, and the matrix $\mathbf{Y}^b$ whose columns are the vectors $\mathbf{y}^{b(i)} - \bar{\mathbf{y}}^b$. This computation is done locally to filter long-distance spurious covariances and to allow for a concurent computation of the analysis at the different grid points on a parallel computer. The local analysis error covariance matrix is estimated by

$$\tilde{\mathbf{P}}^a = [(k-1)\mathbf{I} + (\mathbf{Y}^b)^T \mathbf{R}^{-1} \mathbf{Y}^b)]^{-1} \tag{2.12}$$

and the weights necessary for the computation of the analysis perturbations are computed by

$$\mathbf{W}^a = [(k-1)\tilde{\mathbf{P}}^a]^{1/2}. \tag{2.13}$$

The analysis mean is then obtained by

$$\bar{\mathbf{x}}^a(t_n) = \bar{\mathbf{x}}^b(t_n) + \mathbf{X}^b(t_n)\bar{\mathbf{w}}^a(t_n) \tag{2.14}$$

.

2.4 Coupling strategies

In all four configurations of the coupling considered in this thesis, the global background ensemble is obtained by equation 2.4. In the first three strategies, the coupling is in one direction: the limited area data assimilation process uses information provided by the global analysis at the current or the previous analysis time, but the the limited area analysis has no effect on the global analysis at the current or future analysis times. In the fourth strategy, the global analysis within the limited area domain is prepared using information from the limited area analysis, thus feeding back information from the limited area data assimilation process to the global data assimilation process. In our description of coupling Strategy 4, we make use of the fact that both the mean analysis and the analysis ensemble members can be computed by linearly combining the background ensemble perturbations.

2.4.1 Strategy 1: Limited area analysis by spectral interpolation

The limited area analysis $\bar{\mathbf{x}}_l^a(t_n)$ is obtained by interpolating the global ensemble mean analysis to the higher resolution grid of the limited area model:

$$\bar{\mathbf{x}}_l^a(t_{n-1}) = \mathcal{L}[\bar{\mathbf{x}}_g^a(t_{n-1})]. \tag{2.15}$$

In this configuration (Fig. 2.1), although the global model is run in an ensemble mode, only a single limited area run is prepared using the mean of the global ensemble solution to provide the large scale forcing. In this configuration, the limited area model can outperform the global model if it can develop predictable flow fea-

tures which may not be resolvable in the global model in response to the higher resolution bottom boundary condition in the limited area domain.

2.4.2 Strategy 2: Non-cycled limited area analysis

Members of the global analysis ensemble at t_{n-1} are interpolated to the higher resolution model grid of the limited area model to obtain a limited area analysis ensemble:

$$\mathbf{x}_l^{a(k)}(t_{n-1}) = \mathcal{L}[\mathbf{x}_g^{a(k)}(t_{n-1})], \qquad k = 1, 2, \ldots, K. \tag{2.16}$$

This limited area analysis ensemble is then propagated forward in time using the limited area model to obtain the limited area background ensemble:

$$\mathbf{x}_l^{b(k)}(t_n) = \mathbf{f}[\mathbf{x}_l^{a(k)}(t_{n-1}), \mathbf{x}_g^{a(k)}(t_{n-1}), \mathbf{x}_g^{a(k)}(t_n)]. \tag{2.17}$$

A limited area analysis $\bar{\mathbf{x}}_l^a(t_n)$ is then prepared by applying Eqs.(2.5-2.10) the limited area background ensemble $\{\mathbf{x}_l^{b(k)}(t_n),\ k = 1, 2, \ldots, K\}$. This procedure is repeated at each analysis time. This coupling strategy is summarized in Fig. 2.2. Note that the limited area analysis obtained at time t_n is not used at the subsequent analysis times t_m $(m \geq n)$. In this configuration, the limited area analysis can perform better than in Strategy 1, if the high resolution background ensemble perturbations that develop after a $\frac{3}{2}\Delta t$ [2] time integration of the limited area model, in response to

[2]Because the observations assimilated at time t_n are collected in the time window $t \in [t_n - \Delta t/2, t_n + \Delta t/2]$, the model is integrated for a time $\frac{3}{2}\Delta t$ from t_{n-1} to provide a background trajectory $\mathbf{x}^b(t)$ for the entire observation time window. The observation operator $\mathbf{h}$ operates on this background trajectory.

the combined effects of uncertainties in the lower resolution large scale flow and the higher resolution forcing terms, provide a more accurate estimate of the background error covariance than does the global background ensemble. Such an approach can also improve the limited area forecasts, if it reduces the transient effects that may occur in Strategy 1 due to using a different model (the global model) in the data assimilation process than in the forecast process (the limited area model).

2.4.3 Strategy 3: Cycled limited area analysis

As in Strategy 2, we create the limited area analysis ensemble at the very first analysis time, t_1, by interpolating the members of the global analysis ensemble on the higher resolution grid of the limited area model. We propagate this ensemble forward in time, using the limited area model, and prepare a limited area analysis by applying Eqs. (2.5-2.10). In all subsequent cycles, the limited area background ensemble $\{\mathbf{x}_l^{b(k)}(t_n),\ k = 1, 2, \ldots, K\}$ is obtained by integrating the limited area model from the limited area analysis ensemble $\{\mathbf{x}_l^{a(k)}(t_{n-1}),\ k = 1, 2, \ldots, K\}$ from the previous analysis time, and the limited area analysis ensemble at time t_n is obtained by Kalman filter assimilation of observations, as described in Chapter 2 2.3. In this configuration, the limited area analysis can perform better than in Strategy 2, if the limited area background uncertainties cannot be fully modeled as a rapid response of the smaller scale uncertainties to the global scale analysis uncertainties. In this case, cycling the limited area analysis may result in a more accurate estimation of the state through a more accurate estimation of the background error covariance

matrix of the limited area system. This coupling strategy is summarized in Fig. 2.3.

2.4.4 Strategy 4: Feedback from the limited area analysis to the global analysis

In the three coupling strategies described so far, the global analysis is independent on the limited area analysis both outside and within the limited area domain and can be prepared prior to the limited area analysis. In contrast, in the last strategy we describe, the limited area analysis is prepared first in the limited area domain and the weights $\mathbf{w}_l^a(t_n)$ and $\mathbf{W}_l^a(t_n)$ from the limited area analysis are applied to global background ensemble to obtain the global analysis inside the limited area domain. Outside the limited area domain, the global analysis ensemble is obtained as before, computing the weights based on the global background ensemble. This coupling strategy is summarized in Fig. 2.4.

This strategy introduces a feedback from the limited area analysis process to the global process. An attractive aspect of this approach is that it produces a global analysis ensemble that is consistent with the limited area analysis ensemble, in the sense, that the k-th member of the global analysis ensemble, $\mathbf{x}_g^{a(k)}(t_n)$, and the k-th member of the limited area analysis ensemble, $\mathbf{x}_l^{a(k)}(t_n)$, are obtained by the same linear combination of the background ensemble members. This is appealing because each limited area background ensemble member is dynamically coupled to the global background ensemble member of the same ensemble index [e.g., $\mathbf{x}_l^{b(k)}(t_n)$ is coupled to $\mathbf{x}_g^{b(k)}(t_n)$]; applying the same weights to the limited area and global ensemble members, we ensure that the global analyses $\mathbf{x}_g^{a(k)}(t_n)$ and the analyses of the high

resolution perturbations $\mathbf{x}'^{(k)}_l(t_n)$ are consistent with each other. Other strategies do not share information about weights between different scales.

The feedback may also improve the global analysis in the area near and within the limited area domain. In particular, using the high-resolution model fields to obtain the global analysis may reduce the effect of the representativeness errors in the observations. There are two practical issues that have to be addressed when implementing Strategy 4. First, using the weights from the higher resolution limited area analysis in the global analysis requires an algorithm to map the weights from the high resolution grid to the lower resolution global grid. Second, abrupt changes may occur in the weights near the boundaries of the limited area domain. This can be addressed by implementing a blending process that smooths the changes in the weights near the boundary of the limited area domain (see section 3.3.2).

Finally, we note that it would be particularly interesting to test Strategy 4 on a coupled global limited-area model with two-way nesting; that is, in a system where the high-resolution global solution continuously affects the coarse resolution global solution within the limited area domain (e.g., Harris and Durran (2010)). Unfortunately, while two-way nesting is becoming standard for mesoscale models allowing for multiple nests, there is no readily available two-way nested system for the global-limited-area setting.

Figure 2.1: Schematic illustration of the data assimilation by spectral interpolation of the global analysis to the regional model grid (Strategy 1).

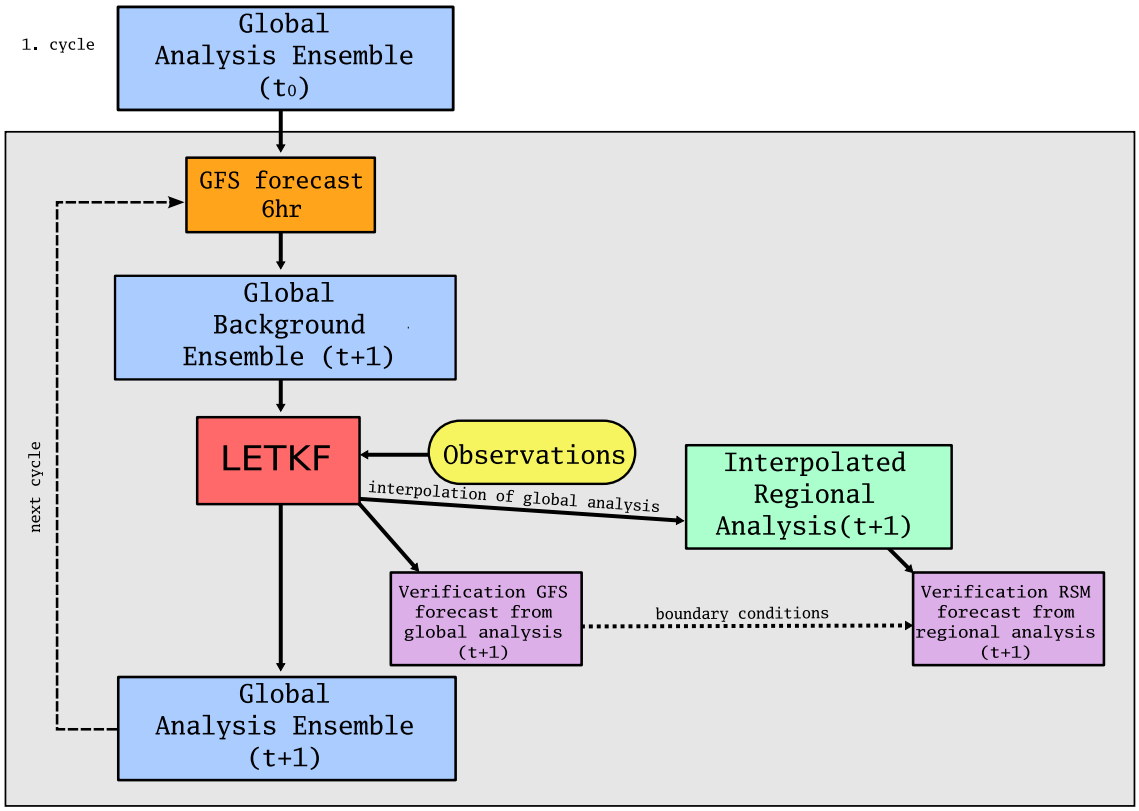

Figure 2.2: Schematic illustration of the non-cycled regional data assimilation Strategy 2 : spectral interpolation of all the global analysis ensemble members to the regional model grid generate a regional analysis ensemble member.

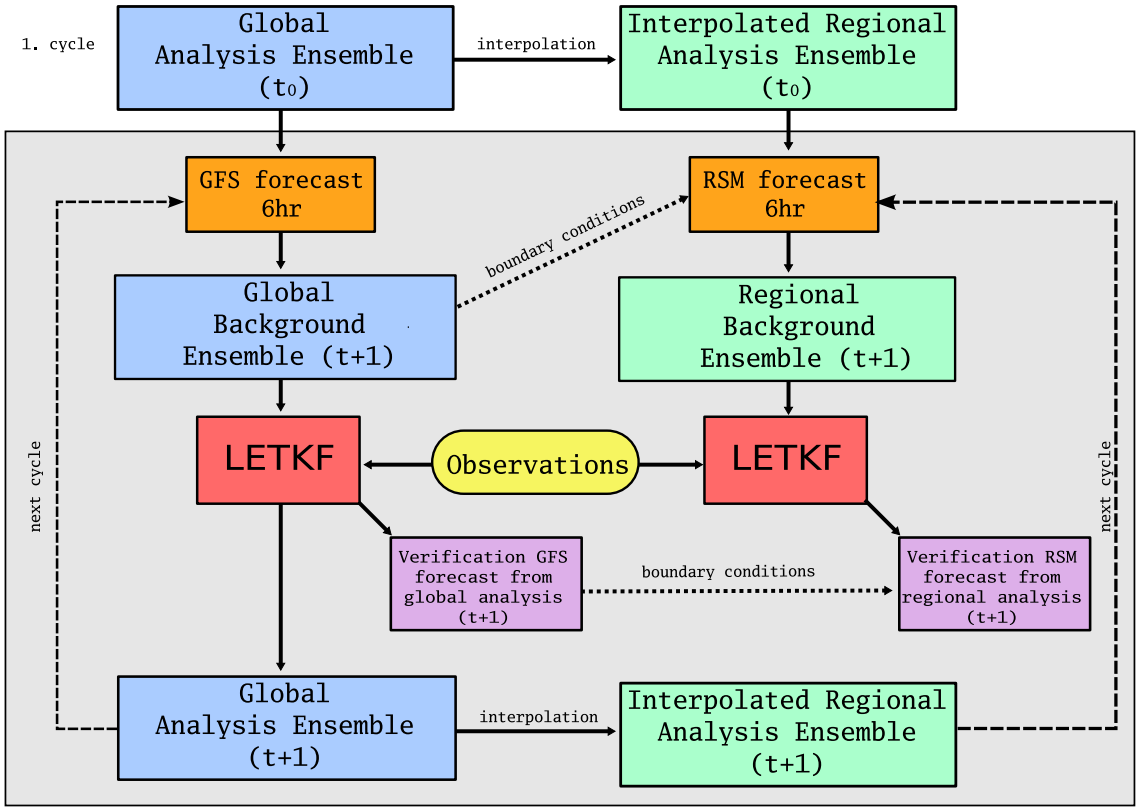

Figure 2.3: Schematic illustration of the cycled regional data assimilation Strategy 3: both the global and the limited area data assimilations are cycled.

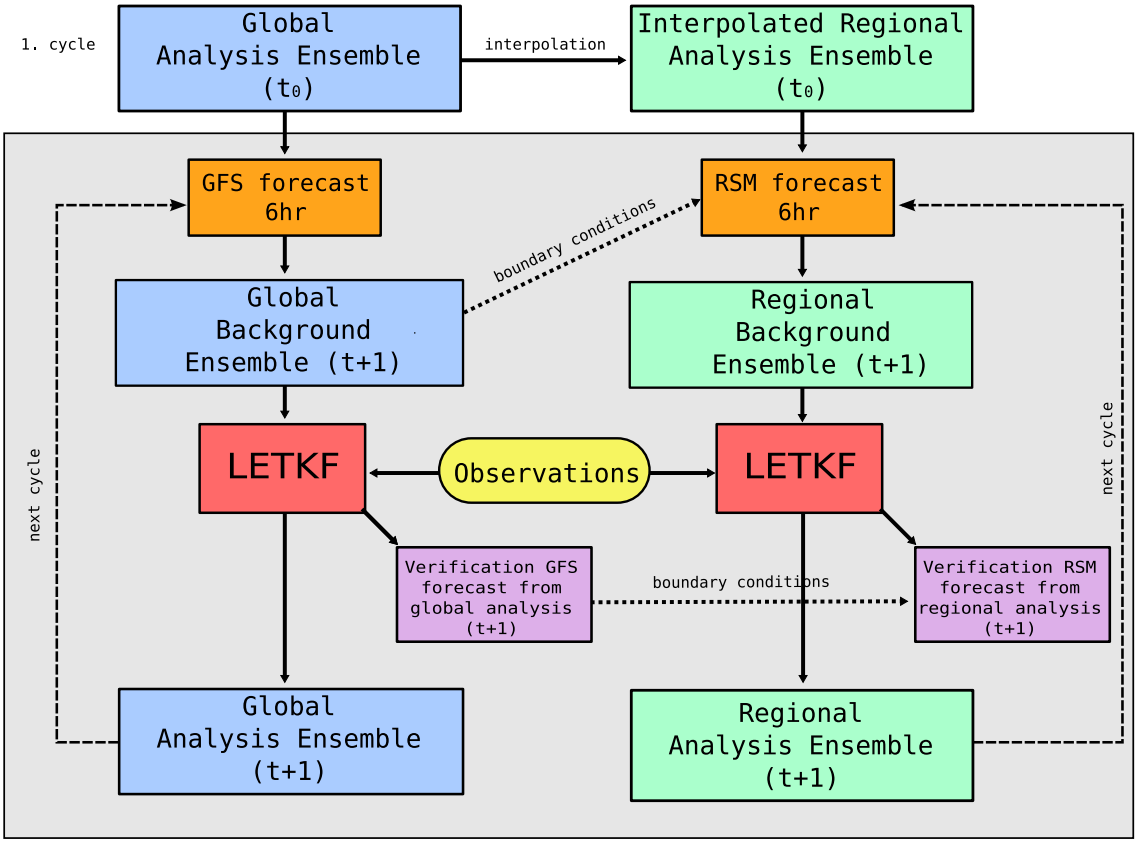

Figure 2.4: Schematic illustration of coupling Strategy 4: both regional and global analysis are cycled, as in Strategy 3, but in the limited area high resolution analysis information is feedback to the global analysis.

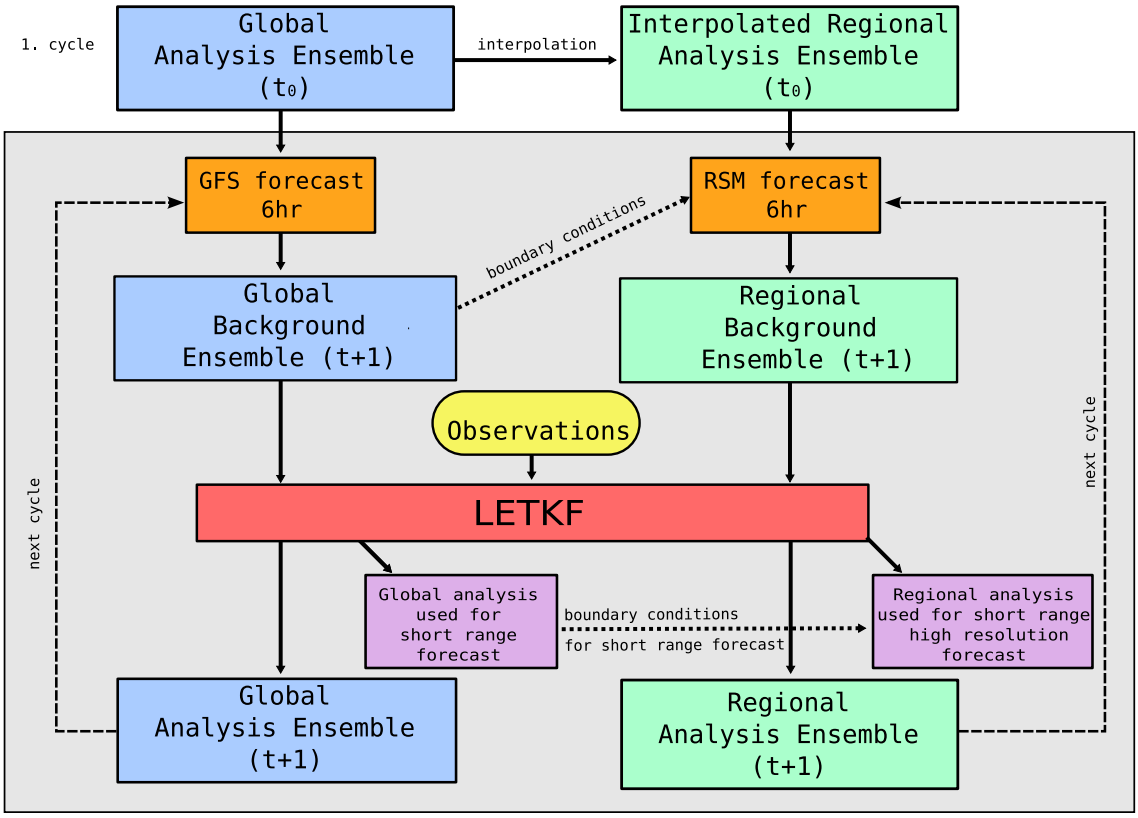

Chapter 3

Experiment design

First, we briefly introduce the three main components of our coupled analysis-forecast system: the global GFS model, the limited area RSM model and the LETKF data assimilation system. Then, we describe the design of the numerical experiments, the observational data sets we assimilate, and the verification scores we use to evaluate the different coupling strategies.

3.1 Model components

3.1.1 GFS

The GFS consists of a model and a data assimilation component, but in this study we use only the model component. The dynamical core of the model is described in Sela (1980). The model has been upgraded numerous times since the nineteen-eighties, mainly to improve the physical parametrization and the computational performance, but the general solution strategy of the dynamical core has remained the same. In particular, the model uses the spectral transform technique to solve the model equations; that is, the nonlinear terms and the terms associated with parametrized physical processes are computed on a grid, while the spatial derivatives are computed in spectral space using spherical harmonics for the rep-

resentation of the atmospheric fields. For vertical discretization the model uses a sigma coordinate system. We integrate the model using a triangular truncation with a cut-off wave-number of 62 and 28 vertical sigma levels (T62L28). At this spectral resolution the nominal resolution of the model (the grid spacing) is about 150 km in the middle latitudes, but-because of the use of a scale dependent diffusion to maintain a realistic kinetic energy spectrum the effective resolution is about 220 km.

3.1.2 RSM

The RSM is a perturbation model. That is, it predicts the evolution of a high resolution perturbation to the lower resolution global model solution and obtains the high-resolution model forecast by adding the forecast perturbation to the global forecast (Juang 1992; Juang et al. 1997). For the computation of the sum of the perturbation and the global fields, the spherical harmonics that represent the global fields in spectral space are directly transformed to the grid points of the NCEP RSM. In our experiments, we use the RSM with a 6-hr nesting period, that is, we store the global model solution with a 6-hr resolution and compute the global fields by a linear time interpolation at each time step of the integration of the RSM.

In the RSM, the time evolution of the perturbation is governed by the linear and nonlinear interactions between the different components of the perturbation and the nonlinear interactions between the perturbations and the large scale flow. The perturbation equation is solved by a spectral transform technique using double

sine-cosine functions to represent the meteorological fields. The vertical coordinate of the model is sigma and the 28 sigma levels of the RSM in our experiments are the same as those of the GFS model. We choose an extended North-American region to be the limited area domain (Fig. 3.1), and we use a horizontal resolution of 48 km in this domain. While the increase of the model resolution with respect to the resolution of the global model may seem to be modest, locally it can lead to a more accurate representation of the orography by $(300 - 500$ meter) (Figure 3.2).

The RSM model offers different options to ensure a smooth transition of the limited area perturbations to zero at the boundaries. We choose the implicit relaxation and blending procedures described in Juang et al. (1997). The blending procedure computes a weighted average of the high resolution forecast and the global forecast, giving increasingly larger weights to the global forecast moving toward the boundaries. We set the blending parameters such that blending affects a total of 20% of the grid points (10 % at each lateral boundary). Thus, since the total number of grid points in the zonal direction is 193, the blending affects 19 points at the eastern and western boundaries and 14 of the 140 grid points in the meridional direction at the southern and northern boundaries. Multiple nesting and non-hydrostatic options are available in the RSM (Juang et al. 1997), but we do not use these features in our experiments.

3.2 LETKF

In the LETKF, the state update step of the Kalman filter is performed independently for each element of the state vector (Ott et al. 2004; Hunt et al. 2007). A key step of the LETKF algorithm is the selection of the set of observations that are considered when updating the estimate of a given state vector component. In practice, the different state vector components at a given grid point are analyzed in one step and in situ observations are selected for assimilation if they are closer to the grid point than a given distance. The assimilation of nonlocal radiance observations with the LETKF is also possible, but for those observations the observation selection is done in a different way (Fertig et al. 2008). In this study, we use the same set of LETKF parameters in both the global and the limited area data assimilation system as was used in the global system described in Szunyogh et al. (2008). The number of ensemble members is $K = 40$. Observations are assimilated if they are within a 800 km radius of the grid point, and the inverse of the assumed observational error variance is tapered linearly from its original value at 500 km to zero between a distance of 500 and 800 km (thus tapering the effects of observations on the analysis that are further away than 500 km). The initial ensemble members are sampled from a free run with the NCEP GFS.

The one important difference between our implementation of the LETKF on the GFS and the RSM is that in the GFS implementation we employ a digital filter (Lynch and Huang 1992) to control free gravity wave oscillations, but we cannot perform such a filtering of the high-resolution limited area fields because a digital

filtering capability is not available for the RSM.

In our implementation of strategy 4, we compute the weights $\mathbf{w}_g^a(t_n)$ and $\mathbf{W}_g^a(t_n)$ for the global analysis within the limited area domain by interpolating the weights from the four closest grid points of the high resolution grid at the same vertical level since both the global and the limited area models have the same vertical resolution. Figure 3.4 shows a randomly selected component of $\mathbf{w}_g^a(t_n)$ (weight) used in the regional and the global analyses and the changes in the weights of the global analysis due to the regional feedback. We find that the blending procedure applied by the RSM to the model fields results in a sufficiently smooth transition of the weights of the global system near the boundaries in strategy 4. Thus, applying a blending algorithm directly to the weights is not necessary. Another reason for smooth transition near the domain boundaries, which are located over ocean, is the lack of observations in these regions.

3.3 Observational data set

The observational data set is identical to the one used in Szunyogh et al. (2008). It includes all conventional (non-radiance) measurements that were operationally assimilated at NCEP between 1 January 2004 at 0000 UTC and 29 February 2004 1800 UTC. Figure 3.5 shows the location of the surface pressure observations on a typical day. In the simulated observation experiments, we use information only about the location and the type of observations from the observation reports to generate simulated observation of the right type at realistic locations by adding

random "observation noise" to a time series of "true" states. To simplify the generation of the simulated observations, we assume that all observations were taken at the analysis time; that is, the random observational noise is added to the true state at the analysis time.[1] This true state is obtained by first generating a time series of coarse resolution global true states with a 60-day integration of the NCEP GFS starting from the operational global analysis of NCEP on 1 January 2004 at 0000 UTC. Then a 60-day integration of the RSM is carried out to add a high resolution perturbation to the true state over the extended North American region. Fig. 3.1 shows the time mean flow in the nature run. One important feature of the time mean flow is the low pressure region over north-east Canada. The limited area model domain includes only part of this stationary low, and, as we will show later, this will obviously degrade the performance of the limited area system in the region north of the 5200 gpm isoline.

Fig. 3.3 shows the difference between the high- and the low-resolution components of the true state for the 500 hPa geopotential height after 16 days of integration. Although the regional model is started from a global analysis and the global component of the high-resolution fields is provided by the NCEP GFS throughout the entire simulation, substantial differences develop between the high resolution true state and its global component inside the limited area domain. For a more

[1]When observations of the real atmosphere are assimilated, we take advantage of the 4-dimensional capabilities of the LETKF (Hunt et al. 2004, 2007); that is, we use background information, regarding both the state and the error covariance matrix, which is valid at the exact observation time.

quantitative assessment of the difference between the high-resolution nature run and its low-resolution global component, we show the kinetic energy spectrum for the $\mathbf{x}'_l(t)$ (Eq. 2.3) perturbation component of the nature run (Fig. 3.6). The spectral analysis takes advantage of the property of $\mathbf{x}'_l(t)$ that it satisfies double-periodic boundary conditions on the limited area domain: The kinetic energy spectrum is obtained by (i) taking the double Fourier transform of the two zonal components of the wind vector, (ii) computing the square of the magnitude of the spectral coefficients by multiplying the spectral coefficients with their complex conjugate, (iii) adding the square of the magnitude for the two components of the wind (iv) summing the squares in unit width wave number bands centering the bands on the integer wave numbers, finally (v) taking the time mean of the spectra. To make the interpretation of the figure easier, we scale the wave numbers by the ratio of the length of the full latitude circle along the globe and the zonal length of the limited area domain. That is, the results from the limited area spectral analysis are shown with respect to the global wave number. The spectral analysis shows that the initially zero perturbation $\mathbf{x}'_l(t)$ develops an energy spectrum that peaks at the synoptic scales (wave number 6-20) and has a relatively large value even at the largest resolved scale of about wave number 4.

3.4 Experiment design

The data assimilation is carried out by first running the global analysis cycle from 1 January 2004 at 00:00 UTC. Then the regional analysis cycle is run from 16

January 2004 at 00:00 UTC. The regional data assimilation period is started only 15 days after the beginning of the global cycle to avoid the propagation of transient effects from the global to the regional assimilation cycle. We prepare global and limited area analyses following the four strategies described in Chapter 2.

3.5 Verification scores

We assess the performance of the different coupling strategies by preparing deterministic global and limited area forecasts for each configuration of the global/local data assimilation coupling. We verify forecasts at the 12-hr and the 48-hr forecast lead times. Since the boundary conditions tend to degrade the limited area forecasts near the boundaries (e.g., Warner et al. 1997; Torn et al. 2006), we define a verification region that is smaller than the limited area domain. (See Fig. 3.1 for the definition of the verification region.) We deem a configuration better if it produces, on average, more accurate forecasts in the verification domain.

In the perfect model experiments, the verification is done against the known true state on the high resolution grid of the RSM. The magnitude of the error of the forecast of a variable at a given time and model level is measured by the root-mean-square error. The mean in the computation of the root-mean-square is taken either over all grid points in the verification domain and all verification times, or over all verification times. In the former case, the error for a given variable and level is a single scalar, while in the latter case, the error is a two-dimensional field in the limited area domain. We also analyze time series of the mean square error at

Figure 3.1: Ilustration of the limited area domain. Green rectangle indicates the boundary of the forecast verification domain. Thin contours show the time mean for the time period of the study (Jan-Feb) of the geopotential height of the pressure level in the "true" states.

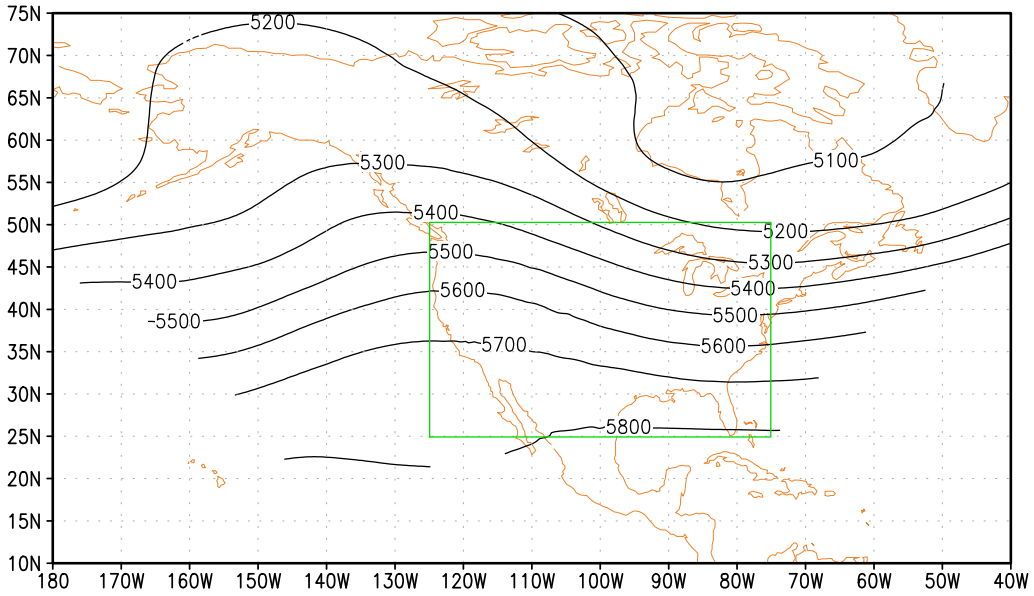

certain model levels.

To verify the forecasts of the real atmosphere, we compute the root-mean-square error of the forecasts against radiosonde observations at the mandatory pressure levels where observations are available for all radiosondes. For the computation of this statistics, the forecasts are interpolated by a bilinear horizontal interpolation to the observation locations and the mean is taken over all observation locations and over all observation times. Since the errors in the forecasts are not correlated with the errors in the radiosonde observations, this verification approach can reliably detect changes in the accuracy of the forecasts that are smaller than the root-mean-square of the observation errors (e.g., Szunyogh et al. 2000).

Figure 3.2: Difference in the orography of the RSM and the GFS models. Thin contours show the height of the orography in the RSM model, while color shades show the height of the orography in the RSM model minus the height of the orography in the GSF.

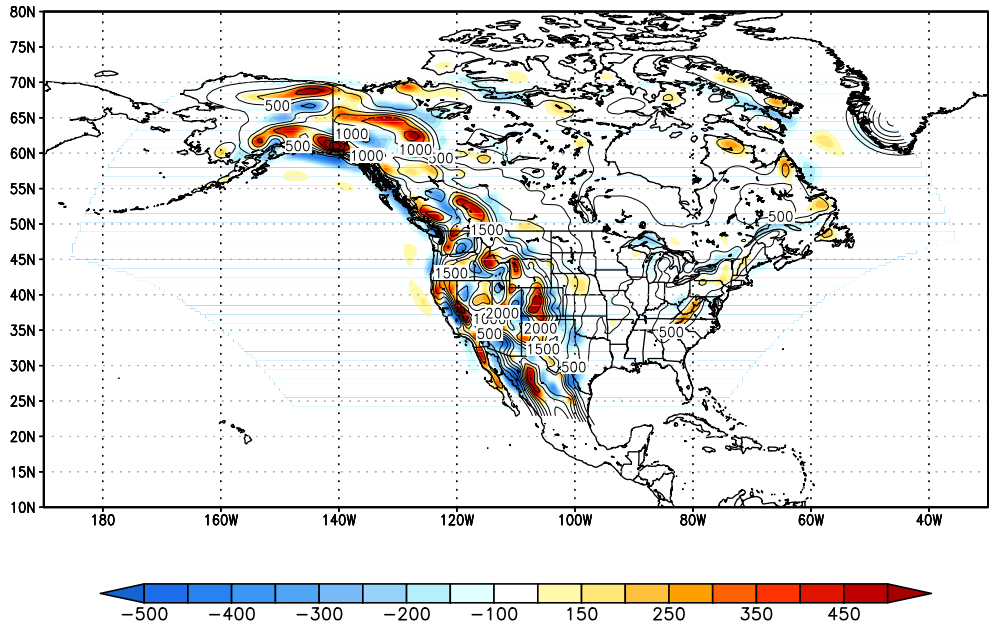

Figure 3.3: A snapshot of the high-resolution perturbation component of the truth in the limited area domain (color shades). Shown is the 500 hPa geopotential height component of the perturbation after 16 days of model integration. Also shown is the low resolution global component of the 500 hPa "true" geopotential height field (contours).

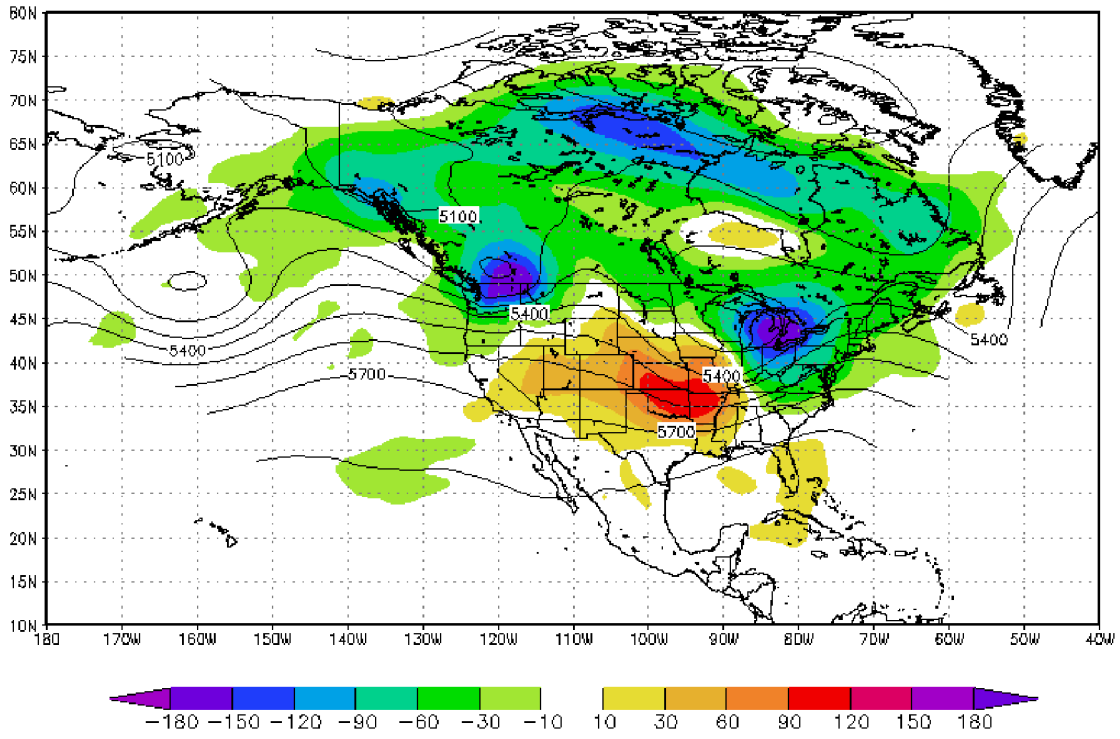

Figure 3.4: A randomly selected component of the weight $\mathbf{w}^a$) for the global analysis (a) and the regional analysis (b). Also shown is the change introduced to the global weights by feeding back information from the limited area analysis (c). Since the global model uses a reduced number of grid points toward the poles, the value of the weight is not available at all plotted locations for the global case.

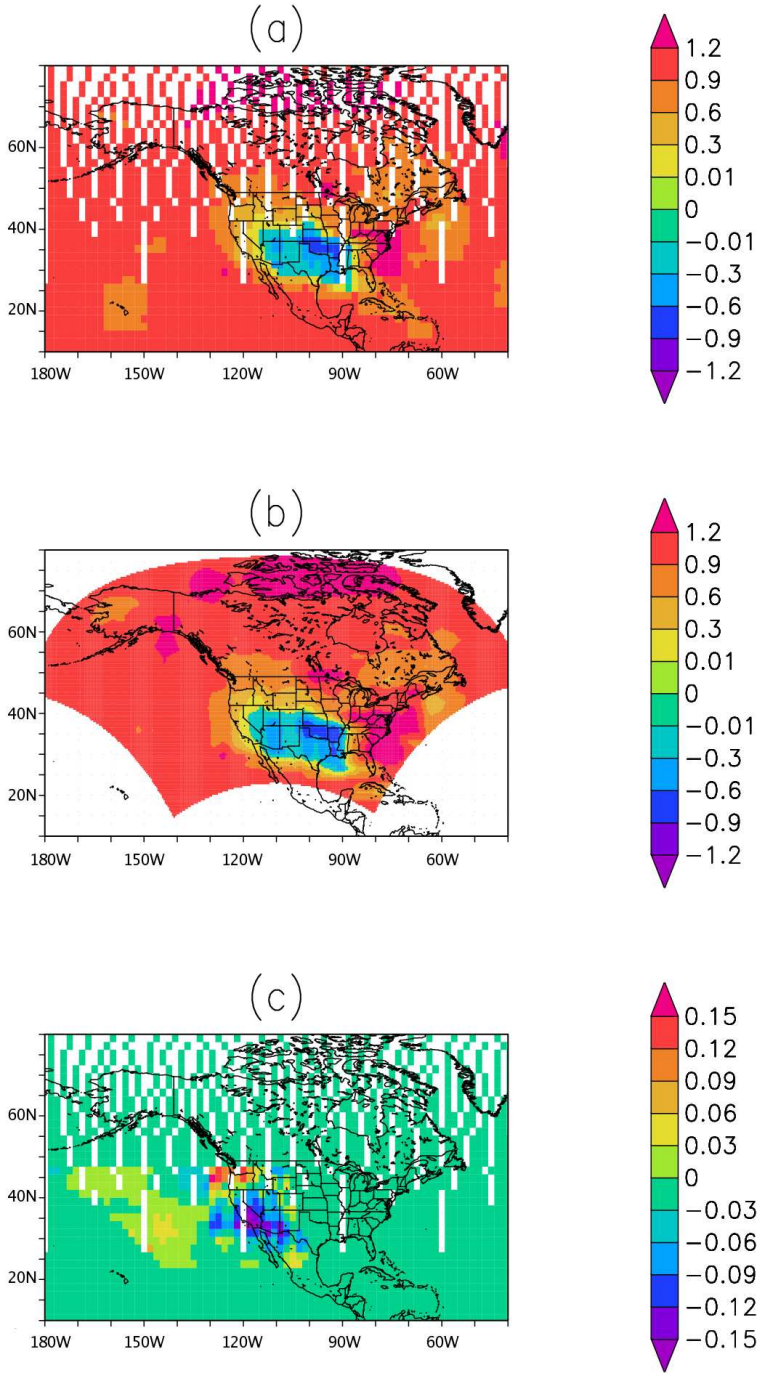

Figure 3.5: Location of the surface pressure observations, January 16 2004 at 00:00 UTC

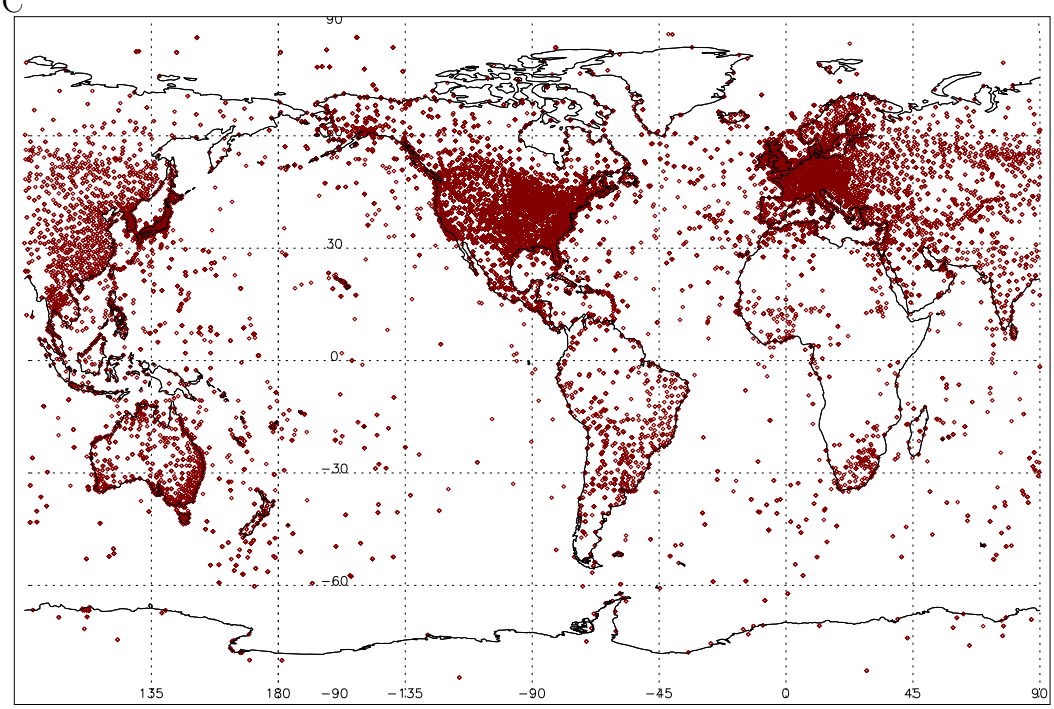

Figure 3.6: The time mean kinetic energy spectrum of the high-resolution perturbation component of the truth with respect to the global wave number (dashes) in a log-log scale. The straight solid line with slope -3 indicates the scaling law for the kinetic energy in the inertial range of two-dimensional turbulence.

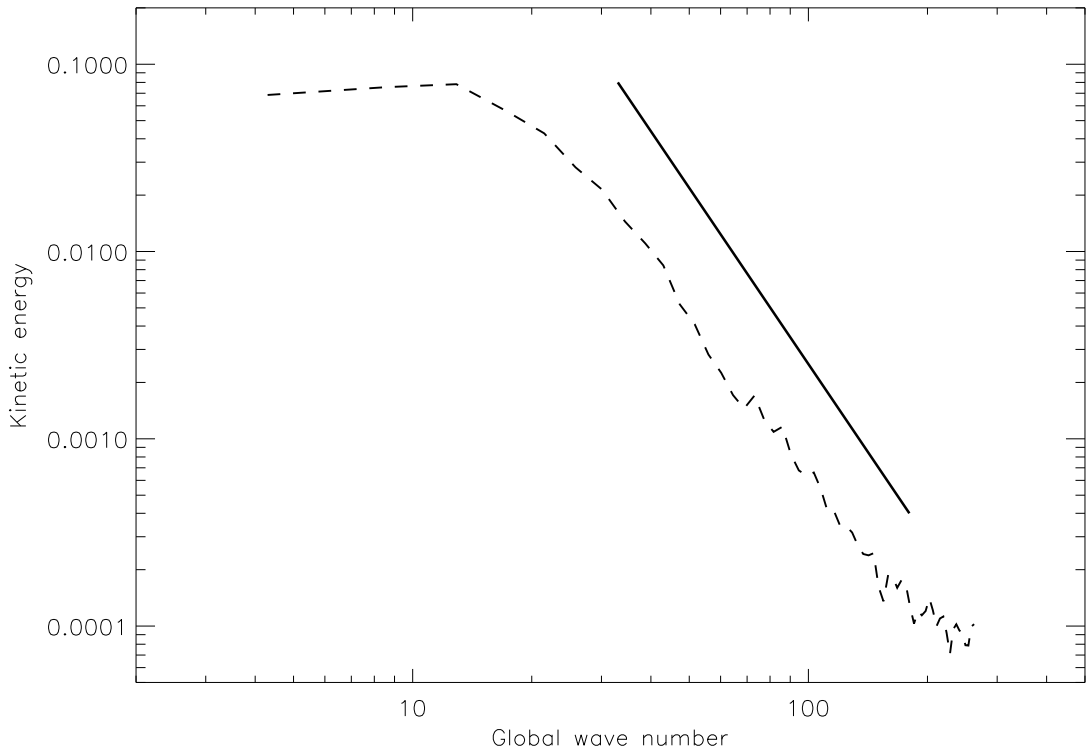

Chapter 4

Results

First, we will assess performance of all strategies under the perfect model assumption. The set of the simulated observations described in 3.3 are assimilated in each analysis step and the results are compared with the "true" state of the atmosphere. To assess the performance of the proposed strategies in a realistic settin,g observations of the real atmosphere are also assimilated and the resulting analyses and forecasts are verified against radiosonde measurements.

4.1 Perfect model scenario

We first compare the performance of the data assimilation systems for Strategies 1-3, where information is not propagated back from the regional to the global analysis. Then we compare the performance of the two systems using Strategy 3 and 4 to study the effect of the feedback.

4.1.1 The comparison of Strategies 1, 2 and 3

In Figure 4.1, we show the vertical profile of the root-mean-square error at 12-hr and 48-hr forecast times for the temperature and the two horizontal components of the wind. The results suggest that all three limited area strategies provide

forecasts that are more accurate than the global forecast. On average, Strategy 3 (regional cycled analysis), provides more accurate forecasts than Strategy 2 (noncycled regional analysis), and Strategy 2 provides more accurate forecasts than Strategy 1 (interpolated global analysis). While all three limited area forecast systems maintain their large advantage over the global system for the entire 48-hr, the difference between the performance of the three limited area systems is smaller at 48-hr than at 12-hr forecast time. Figure 4.2 shows the time evolution of the spatial mean of the root-mean-square forecast error at 12-hr forecast time in the limited area domain for temperature and wind at 500 hPa. The agreement with the conclusion drawn based on the vertical profiles, Strategy 3 (cycled regional analysis), performs clearly better than the other strategies.

We show the spatial distribution of the forecast improvements introduced by the increasingly more sophisticated limited area data assimilation processes for the geopotential height at 300 and 500 hPa (Figures 4.3 and 4.4) and for the temperature at 850 hPa pressure level (Figure 4.5). Using the limited area model only to prepare the forecasts (Strategy 1) consistently improves all verified forecast parameters in the verification domain (see panels a and d of the Fig. 4.3-4.5). Evolving the background ensemble for a single assimilation cycle with the limited area model (Strategy 2) has little additional value compared to Strategy 1 (panels b and e); while cycling the limited area assimilation (Strategy 3) leads to major improvements compared to Strategy 2. While the system based on Strategy 3 performs best in the verification domain, it also has obvious difficulties outside the verification domain, near the northern and western lateral boundaries of the limited area domain. This result

suggests that while propagating the background covariance information with the limited area model is beneficial in general, propagating the covariance through the boundaries can be problematic even in the perfect model scenario.

4.1.2 The comparison of Strategies 3 and 4

Area averaged errors are shown for Strategy 3 and 4 in Figure 4.6, but we do not find these differences statistically significant. (We tested the statistical significance of the difference between the errors for the two strategies by the procedure described in Szunyogh et al. (2008).) The vertical profiles of the forecast errors shown in 4.6 suggest that Strategy 4 (feedback) has a small negative effect on both the global and the limited area forecast. Thus the conclusion is corraborated by Figure 4.7 which shows the time evolution of the 12-hr root-meen-square forecast error for three different variables at 500 hPa. Figure 4.8 shows that Strategy 4 improves the limited area forecasts within the verification region and outside the verification region near the western boundary of the limited area domain, but it degrades the forecasts north of the verification region (panel a, b, and c). This result indicates, that while Strategy 4 has the potential, in general, to improve the limited area forecasts in regions where the limited area domain captures only a part of an important large scale forecast feature, feeding back information from the limited area system can have negative effects. The right hand side panels of Fig. 4.8 (panels d, e, and f), which show the effect of the feedback on the global analysis in the limited area domain, indicate a dominantly negative effect on the global forecasts of the feedback

on the global forecast.

4.1.3 Spectral analysis

Figure 4.9 shows the spectral distribution of the error in the zonal wind forecasts for strategies $1, 2$ and 3 at the 12-h and the 48-h forecast times. This figure is produced by the same procedure as Fig. 3.6, except that the Fourier transform is applied to the errors in the high-resolution wind forecast perturbation. Since the global component of the forecast is the same for all three strategies, this figure illustrates the differences between the spectral distribution of the error in the limited area perturbation component of the forecast for the three strategies. Results are not shown for Strategy 4 because in that case the difference between errors in the large scale forecasts also contributes to the difference between the errors.

The most striking feature of Fig. 4.9 is the large advantage of the system that cycles the limited area analysis (strategy 3) at 12-hr forecast time in the wave number range 10-30. This result indicates that the LETKF coupled with the RSM can more skillfully predict the covariance in the wave number range $10-30$ when the analysis is cycled. At 12-hr forecast time, the difference between the performance of the different configurations of the system is small at the longest resolved scales (wave numbers larger than 10) and at the shortest resolved scales (wave numbers larger than 60). There is no real difference at 48-hr between the performance of the three configurations, with the exception of a slight advantage of the cycled system (Strategy 3).

4.2 Results with observations of the real atmosphere

4.2.1 Comparison of Strategies 1, 2, and 3

Verification results for our analysis-forecast experiments using observations of the real atmosphere are shown in Fig. 4.10. Overall, the limited area systems perform slightly better than the global system at 12-hr forecast time, while the global system performs better than the limited area systems at 48-hr forecast time. The difference between the performance of the limited area systems and the global system is larger for the two components of the wind than for the temperature. In particular, the clear advantage of the limited area systems for the zonal component of the wind below the 300 hPa level at 12-hr lead time turns into a clear disadvantage by the 48-hr forecast time. Another interesting feature of the verification results for the two components of the wind is the big advantage of the global system in the upper troposphere (above 300 hPa), most of which disappears by 48-hr forecast time.

Similar to the results for the perfect model scenario, there is not much difference between the systems based on the different coupling strategies at 48-hr lead time. However, the picture is very different from what we observed for the perfect model scenario at 12-hr forecast time: Strategy 3, which performed the best under the perfect model scenario, performs the worst in the realistic case, while Strategy 2 maintains its slight advantage over Strategy 1. This suggest that the RSM at the tested resolution is not a sufficiently better model than the GFS in the selected limited area to compensate for the problems that arise at the boundaries in Strategy 3.

4.2.2 Comparison of the Strategy 3 and 4

The comparison of the performance of Strategies 3 and 4 with real observations is shown in Fig. 4.11. In these figures, we show the impact of the feedback on both the limited area and the global forecasts (the two curves without feedback are the same as in Fig. 4.11). We note that some caution should be exercised when interpreting the results shown in this pair of figures: the difference between the errors shown in these figures are statistically not significant when tested using the approach of Szunyogh et al. (2008). That test compares the time (sample) mean of the instantaneous differences between the root-mean-square-errors for variance of the two configurations at the various verification times to the variance of the same differences. The failure of the test indicates that the differences in the errors are not due to consistent differences at the different verification times. Instead, they are the net result of differences in the forecast errors, which are highly variable in magnitude and sign.

Interestingly, at 12-hr forecast time, the feedback has a much larger effect on the performance of the global forecast than on the performance of the limited area forecast. In particular, while the global forecasts of the temperature is clearly degraded by the feedback above 300 hPa and below 700 hPa, and the two horizontal wind components above 500 hPa are clearly degraded, the feedback improves the global forecasts of the two wind components in the lower troposphere (below 500 hPa). At 48-hr lead time, the best of the four forecasts is clearly the global forecast without feedback. The only parameters for which this system is not the best are

for the meridional component of the wind in the jet layer (around 300 hPa), where the limited area system with feedback is the best, and for the zonal component of the wind at the bottom of the atmosphere, where the two systems with feedback are the best. Also, at 48-hr lead time the differences are larger between the performance of the two limited area systems. In particular, the system with feedback performs better for the meridional wind component in the jet layer and for the zonal wind below 800 hPa, and it performs worse for the temperature and the zonal component of the wind at the bottom of the atmosphere.

4.3 Conclusions

This thesis documents the first attempt at exploring the potential benefits of coupling the global and limited area ensemble Kalman Filter data assimilation. To the best of our knowledge, ours is the first study that considers a feedback from the limited area data assimilation process to the global process. We carried out analysis–forecast experiments under a perfect model scenario, where the limited area model was considered to be perfect in the limited area domain and the global model errors were considered to be perfect elsewhere. We also carried out experiments in a realistic setting. Our most important findings for the perfect model scenario are the following:

- In the limited area domain, the limited area systems based on the different coupling strategies perform better than the global system. The advantage of the limited area systems is much larger at 12-hr lead time than at 48-hr lead

time.

- Preparing a limited area analysis with a cycled limited area system enhances the performance of the limited area forecast system. The main benefit of cycling the limited area analysis is that it provides better 12-hr lead time forecasts at the synoptic and sub-synoptic scales (global wave number 10-30). A single analysis cycle does not provide sufficient time to achieve a similar effect.

Additional findings from our tests using real atmospheric data are the following:

- The results with observations of the real atmosphere confirms that the limited-area data assimilation has potentially larger benefits at the shorter forecast times (12-hr vs. 48-hr in our experiments). The advantage of the limited area systems is smaller than in the perfect model scenario at 12-hr forecast time but diminishes at 48-hr forecast time.

- Our attempt to feed back information from the limited area analysis to the global analysis led to mixed results. The feedback improved the 48-hr high resolution wind forecast under the perfect model scenario and the meridional large scale wind forecast at 48–hr in the realistic scenario, but also led to considerable degradation of some of the other verified atmospheric variables.

We emphasize that we consider the current study only to be the first step toward exploring the benefits of coupling the global and limited area data assimilation process. One potential extension of this study would be to increase the ratio of the

resolution of the two models from the current 1:4 ratio (48 km vs. about 220 km). Since, in the current system, the cut-off wave number for both models is within the inertial range of two-dimensional turbulence, the regional model does not really bring in new physics compared to the global model. Increasing the resolution of the limited area model to a range where some of the non-hydrostatic processes are explicitly resolved would bring in a new source of kinetic energy (convection), as well as the effects of three-dimensional turbulence. Bringing in new physics could reduce the representativeness component of the observation errors with respect to the limited area model dynamics. This, in turn, could be expected to increase the potential benefits of feeding back information from the limited area data assimilation system to the global data assimilation system. One particular area of research where we expect such an approach to be especially beneficial is in investigating the interactions between a tropical cyclone and the large scale flow. We are currently in the process of testing our coupled data assimilation system for such a scenario.

Figure 4.1: Vertical profile of the root-mean-square forecast error in the limited area domain at 12-hr (a) and 48 (b) forecast time for the global forecast (red solid) and for the limited area forecasts with coupling Strategies 1 (orange long dashes and dots), 2 (blue short dashes) and 3 (green dots).

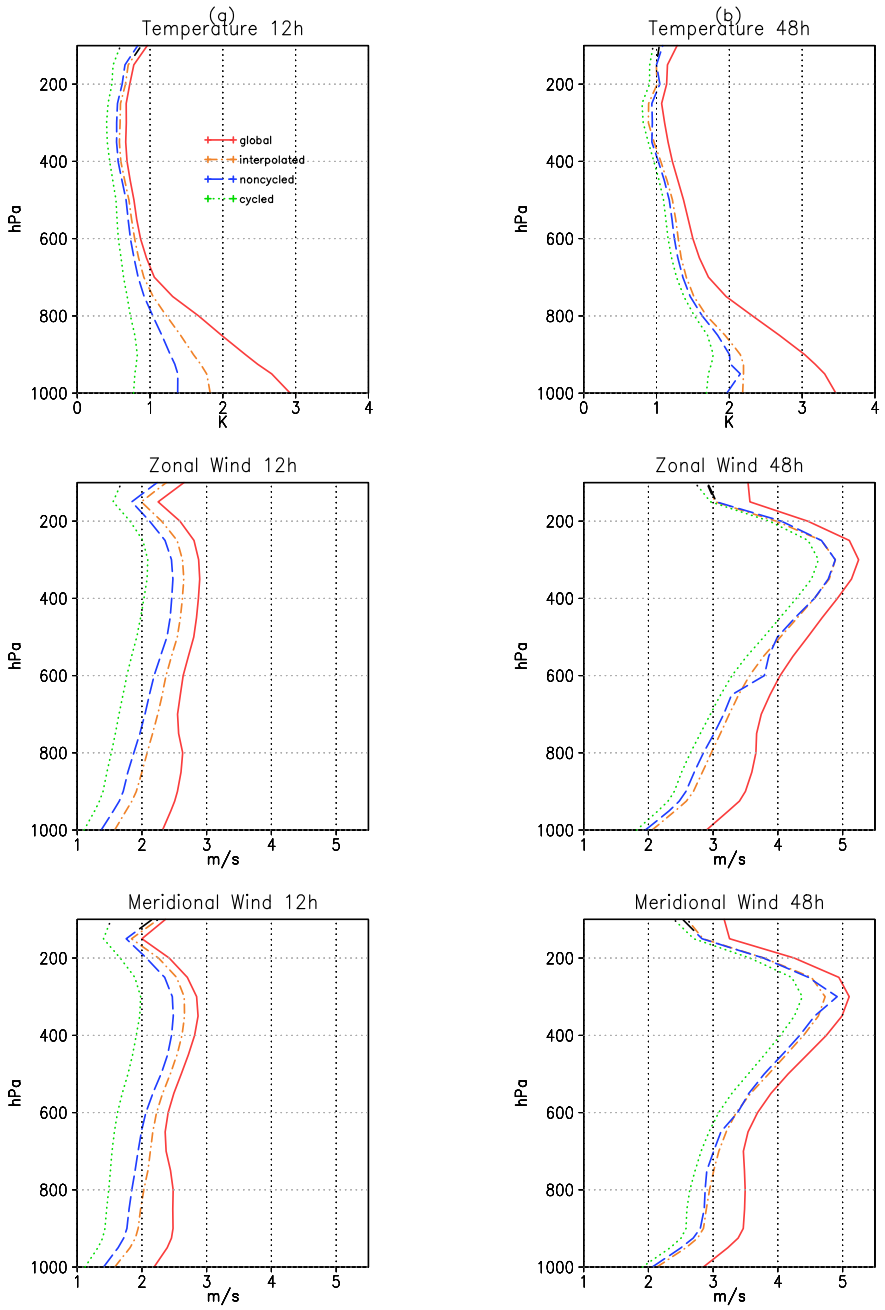

Figure 4.2: Time evolution of the root-mean-square forecast error in the limited area domain at 12-hr forecast time for (a) temperature (b) zonal and (c) meridional wind for the global forecast (red solid) and for the limited area forecasts with coupling Strategies 1 (orange long dashes and dots), 2 (blue short dashes) and 3 (green dots).

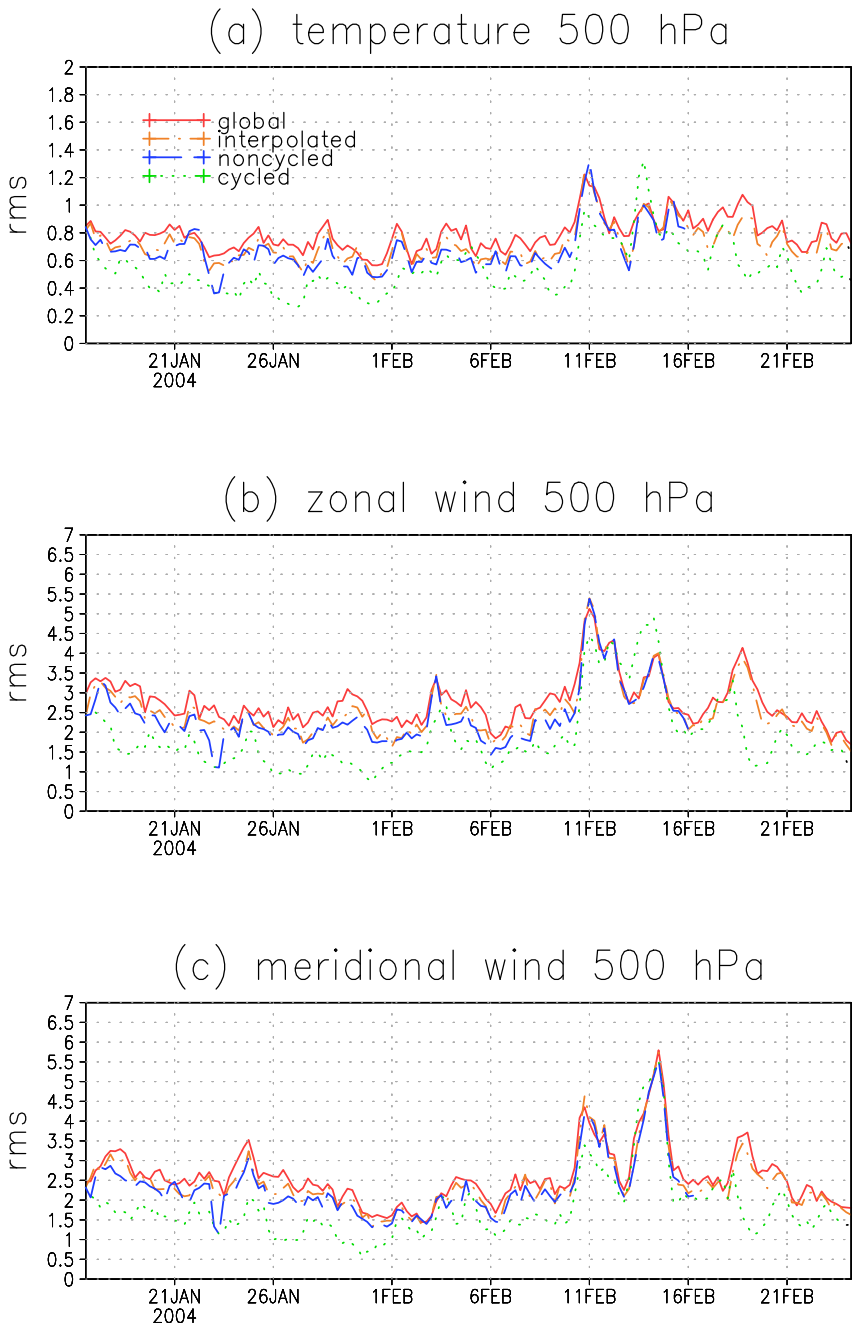

Figure 4.3: The difference between the root-mean square errors of the geopotential height forecasts at the 300 hPa level for the different configurations of the analysis system at 12-hr and 48-hr lead times. Shown are the differences between the forecasts started from the global analysis and the limited area analysis of Strategy 1 (panel a and d), from the limited area analyses of Strategies 1 and 2 (panel b and e), and from the limited area analyses of Strategies 2 and 3 (panel c and f). Where the values are positive, the forecast from latter analysis is more accurate. Also shown is the mean flow at the 300 hPa level for the "true states" in the verification period (contours).

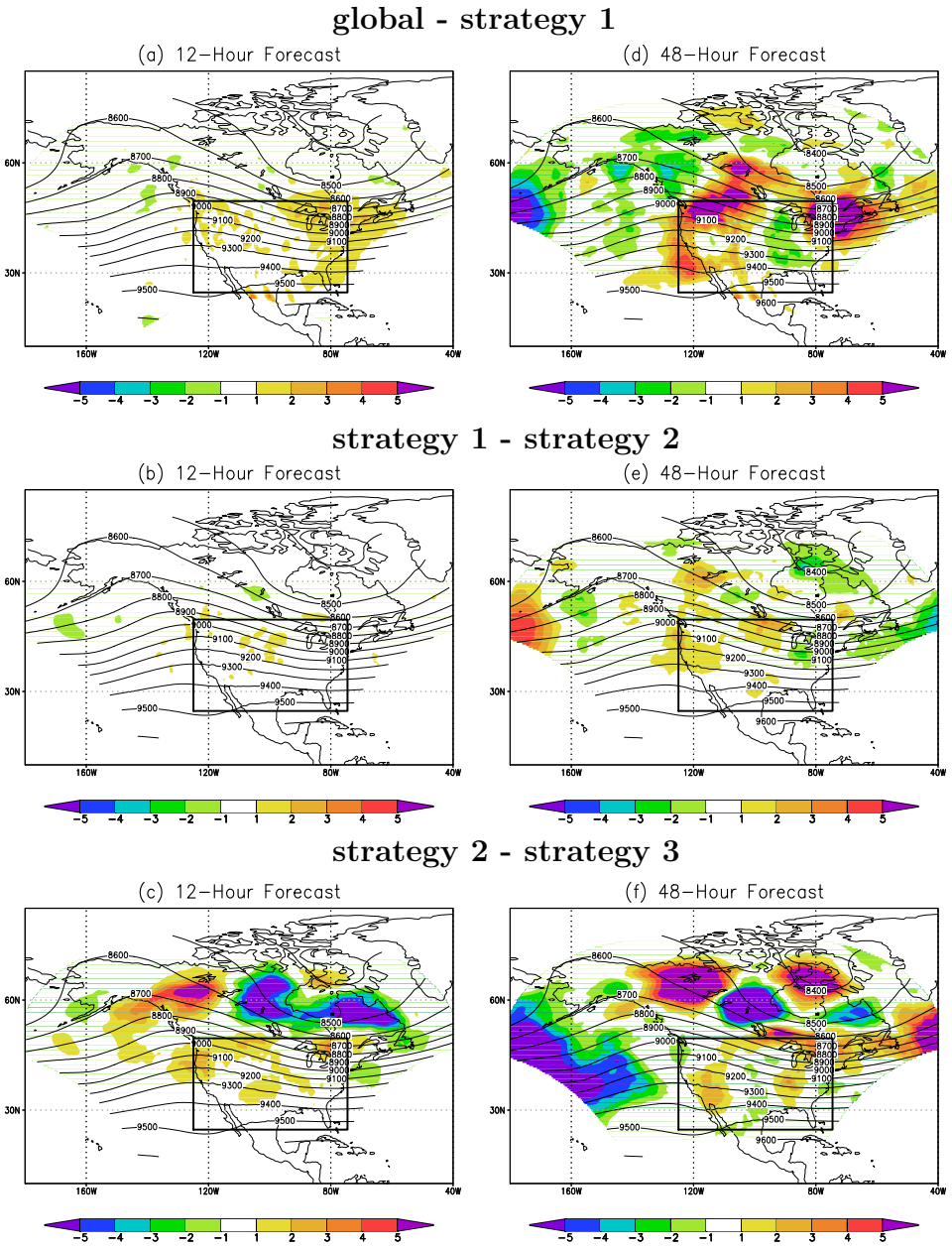

Figure 4.4: Same as Fig. 4.3, except for the geopotential height forecast at the 500 hPa level.

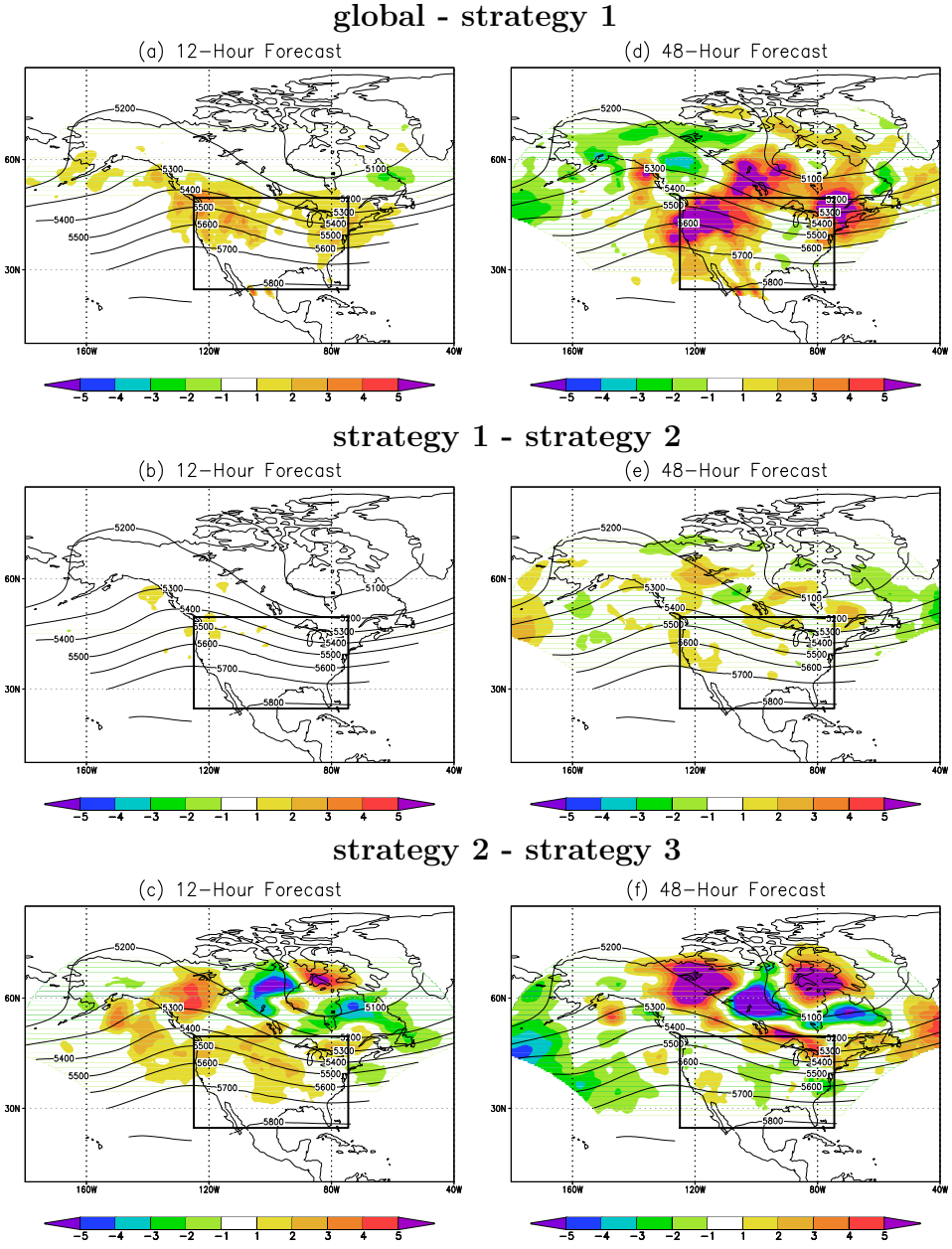

Figure 4.5: Same as Fig. 4.3, except for the temperature at the 850 hPa level.

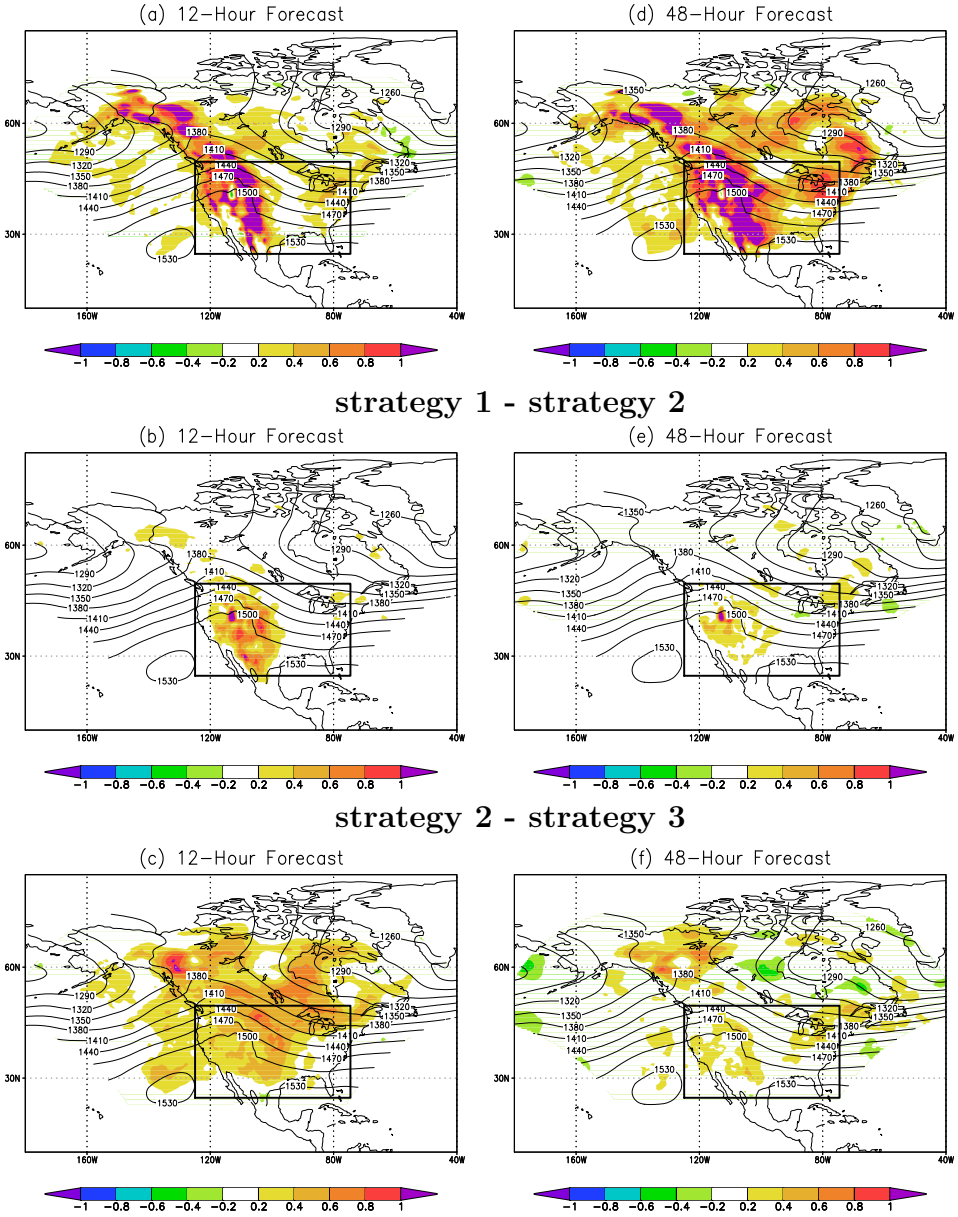

Figure 4.6: Vertical profile of the root-mean-square forecast error in the limited area domain at 12-hr (a) and 48 (b) forecast time for the global forecast (red solid), global forecast with limited area feedback (cyan long dashes and dots), and the limited area forecasts with coupling Strategies 3 regional (green short dashes) and 4 (purple dots).

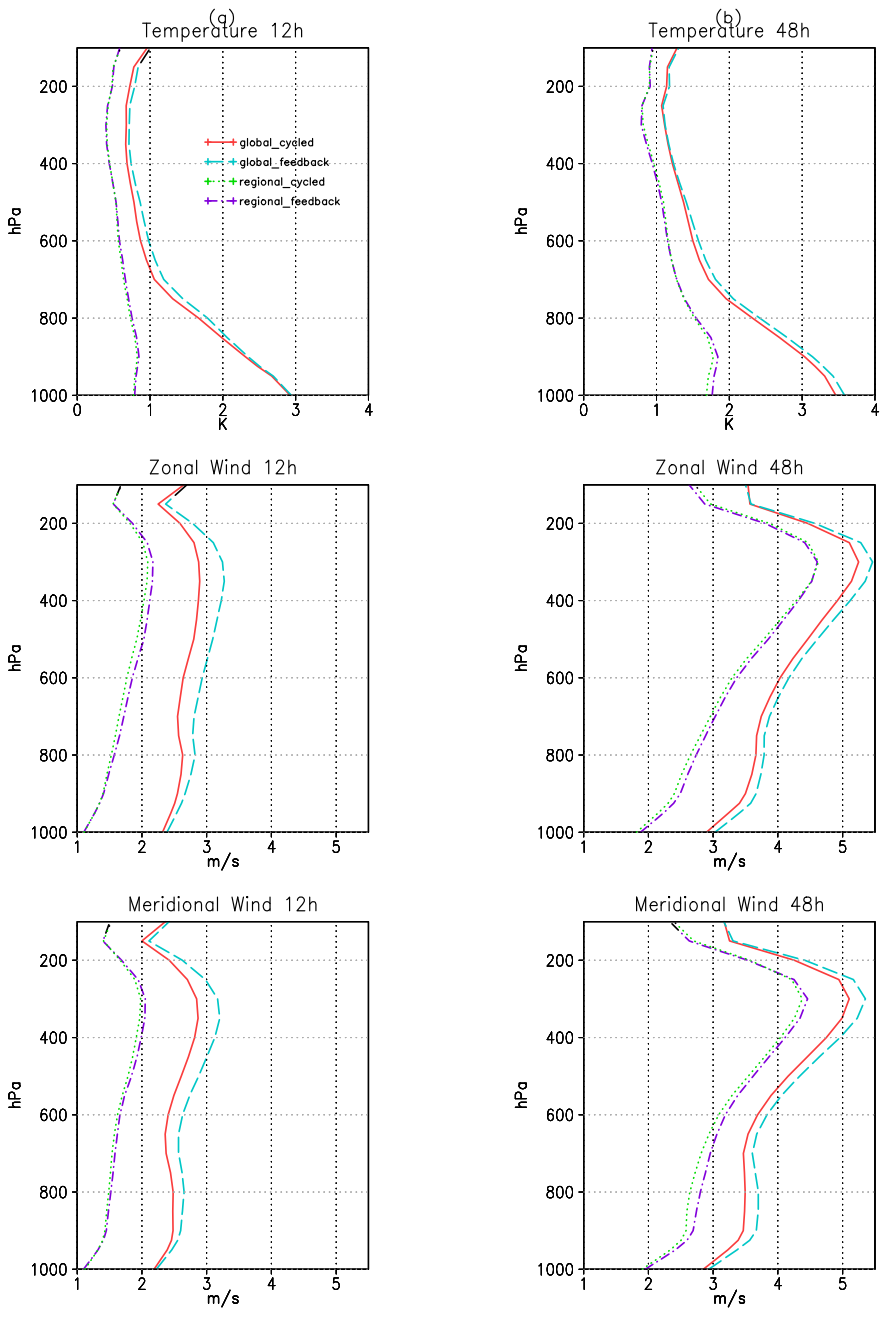

Figure 4.7: Time evolution of the root-mean-square forecast error in the limited area domain at 12-hr forecast time for (a) temperature, (b) zonal, and (c) meridional wind for the global forecast (red solid) and for the limited area forecasts with coupling Strategies 3 and the global forecast (cyan long dashes), and limited area forecasts (dashed purple) with coupling Strategies 4 .

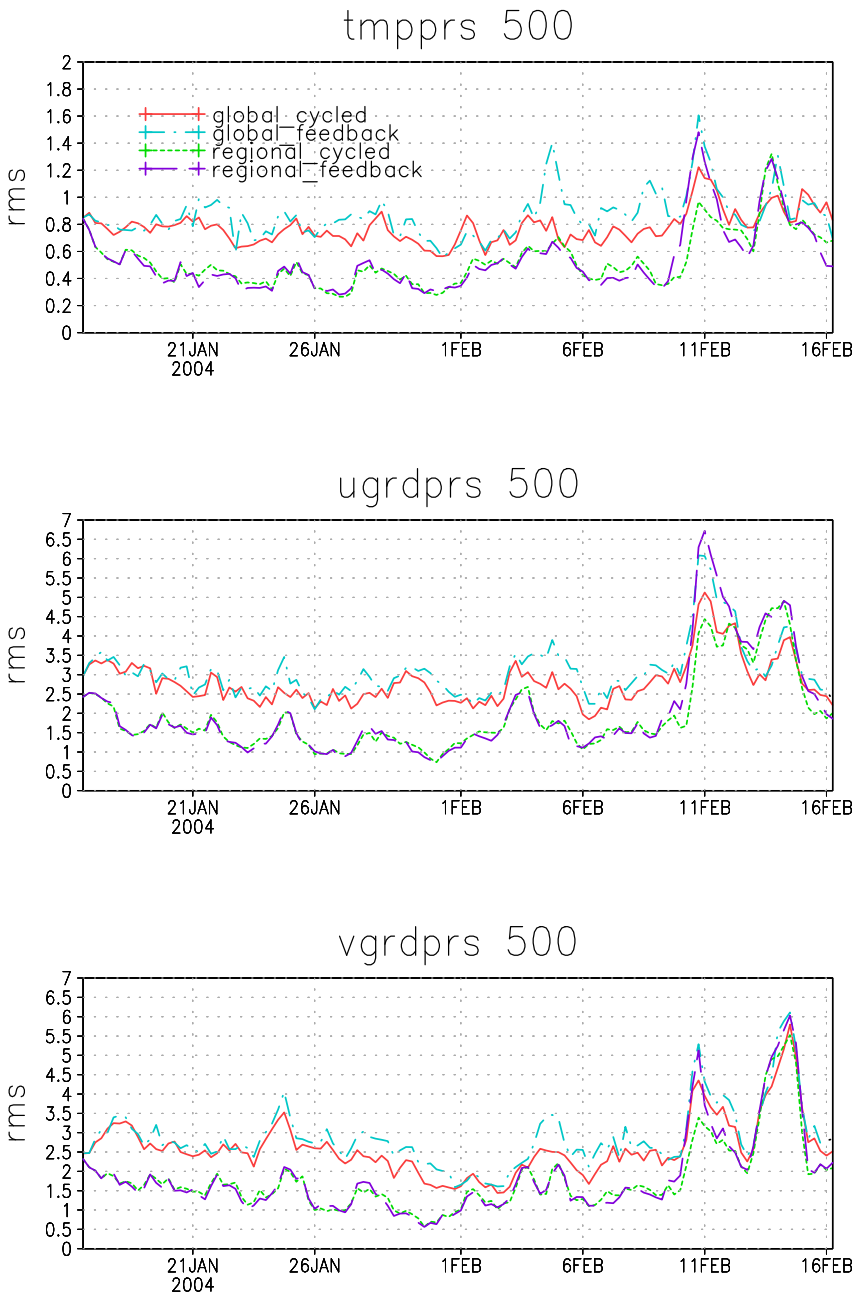

Figure 4.8: The difference between the root-mean square errors of the 48-hr forecasts started from the analyses obtained by Strategy 4 and Strategy 3. Results are shown for the limited area geopotential height forecasts at the 300 hPa (panel a) and the 500 hPa (panel b), the limited area temperature forecasts at 850 hPa (panel c), the global geopotential height forecasts at 300 hPa (panel d) and 500 hPa (panel e), and the global temperature forecast at 850 hPa (panel f). Strategy 4 provides more accurate forecasts where the shades indicate positive values. Contour show the time mean of the true geopotential height at the given level.

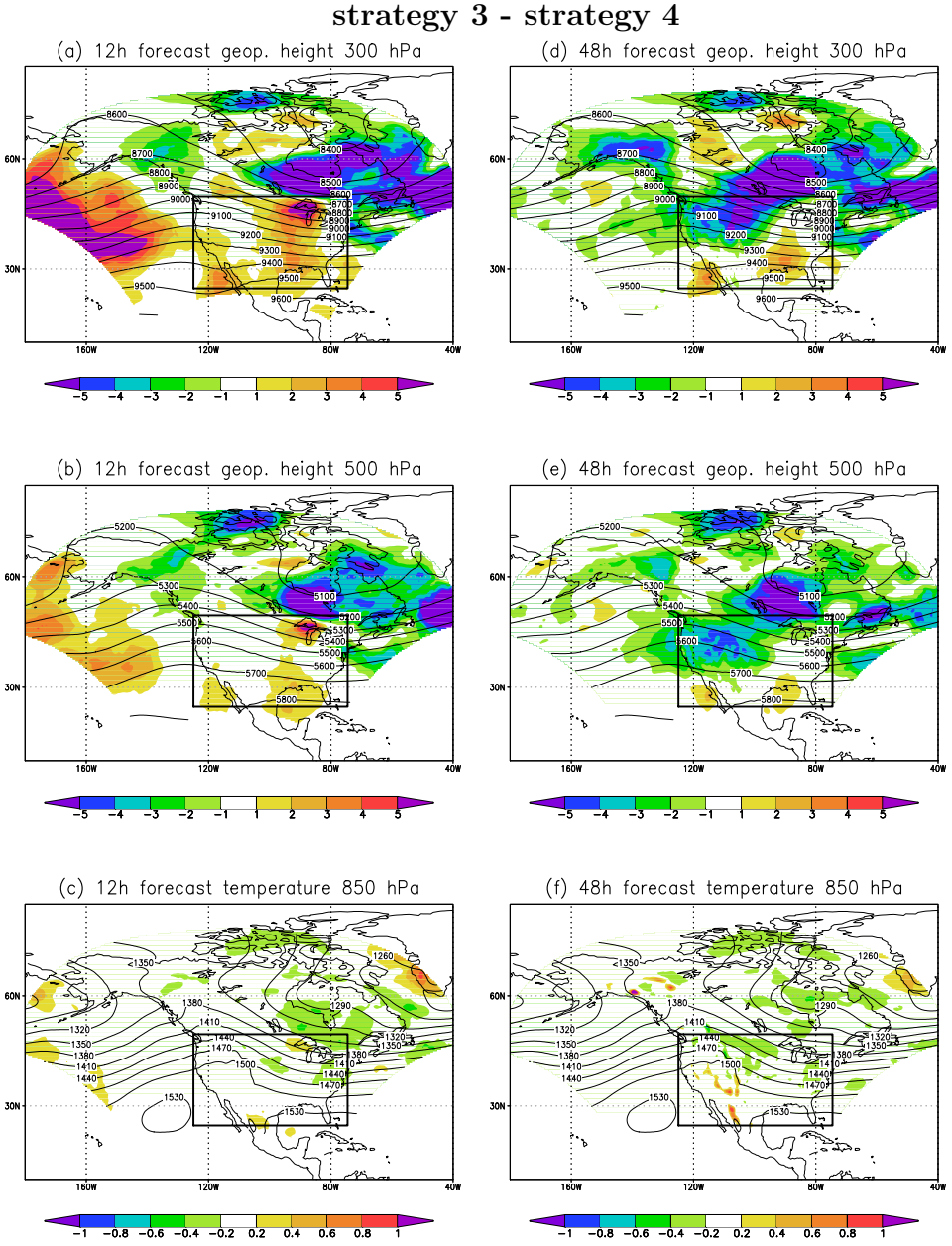

Figure 4.9: The kinetic energy spectrum of the forecast error with respect to the global wave number at 12-hr and 48-hr forecast lead times in a log-log scale. Shown is the error for Strategy 1 (orange), Strategy 2 (blue) and Strategy 3 (green). The straight solid line with slope -3 indicates the scaling law for the kinetic energy in the inertial range for two-dimensional turbulence.

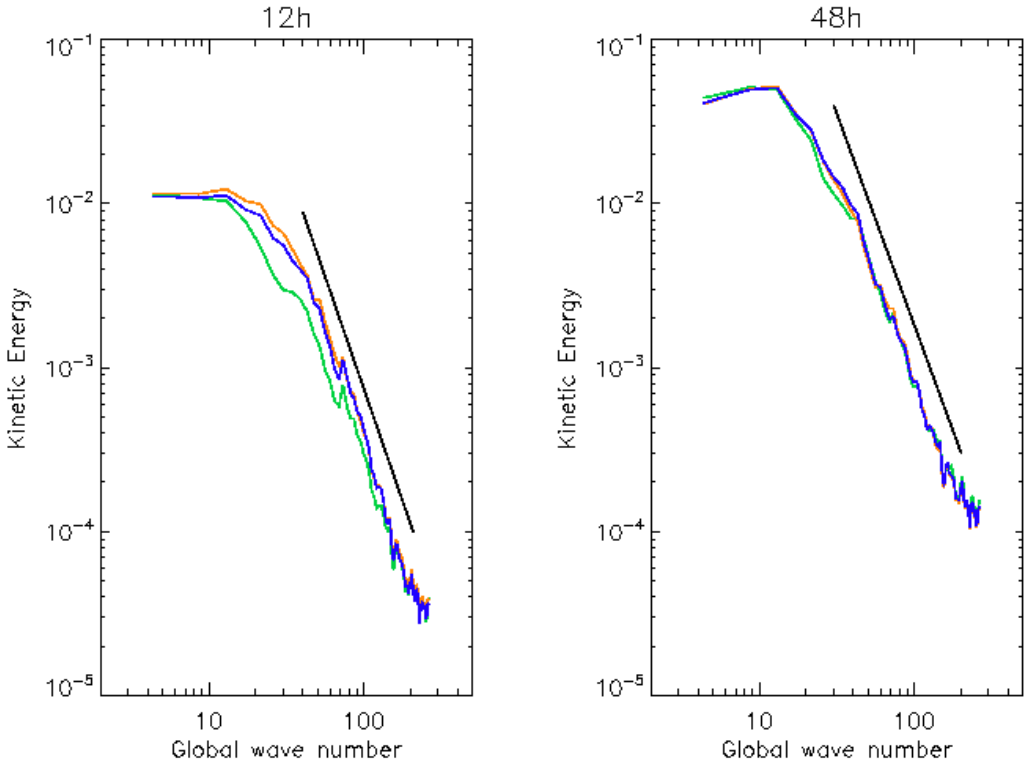

Figure 4.10: Vertical profile of the root-mean-square forecast error in the limited area domain at 12-hr (a) and 48-hr (b) forecast time for the global forecast (red solid) and for the limited area forecasts with coupling Strategies 1 (orange dashes and dots), 2 (blue dashes) and 3 (green dots) assimilating observations of the real atmosphere.

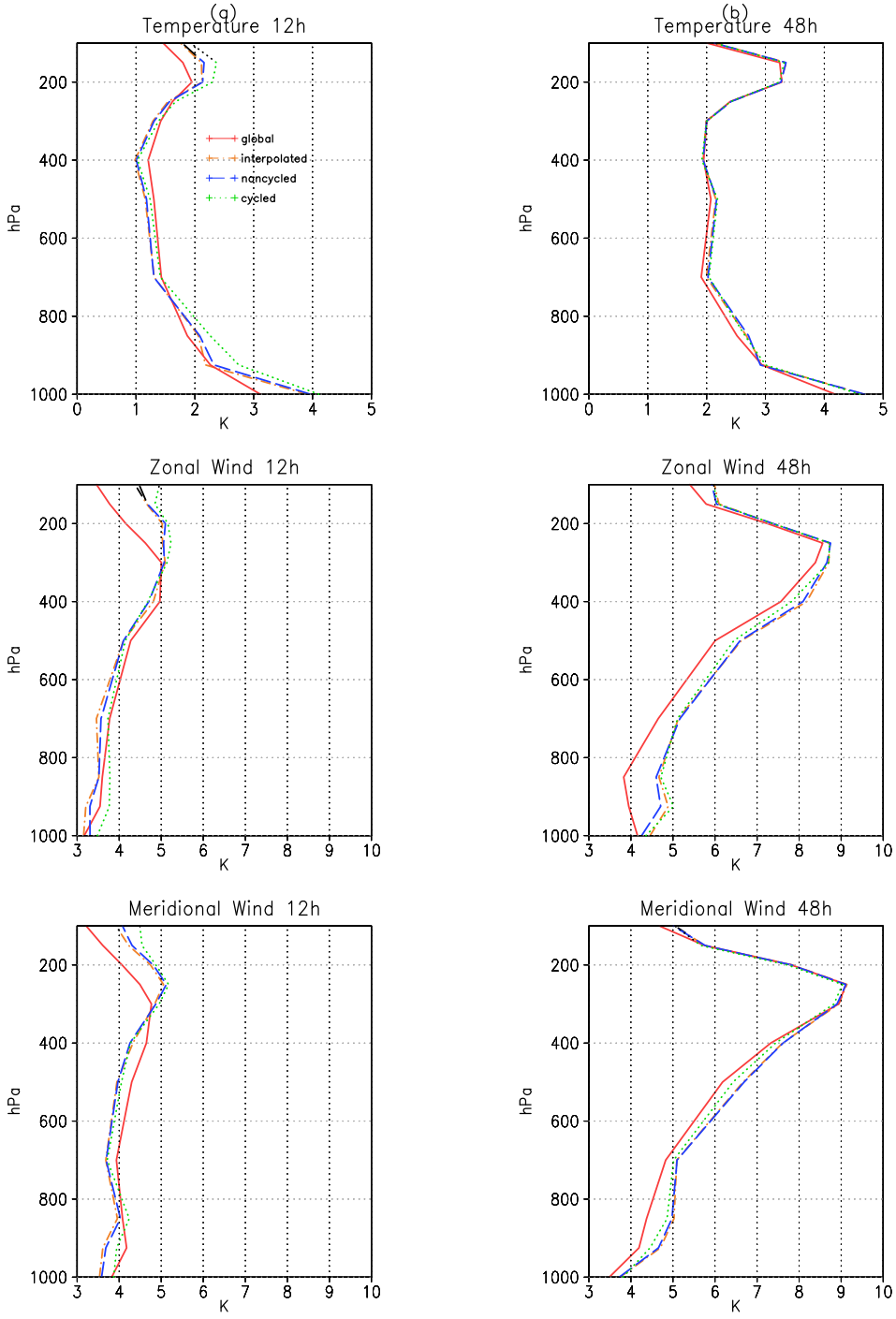

Figure 4.11: Results for experiments assimilating observations of the real atmosphere. Vertical profile of the root-mean-square forecast error in the limited area domain at 12-hr (a) and 48-hr (b) forecast time for the global forecast (red solid), the global forecast with Strategy 4 (cyan dashes), the limited area forecast for Strategy 3 (green dots), and the limited area forecast Strategy 4 (purple dashes and dots).

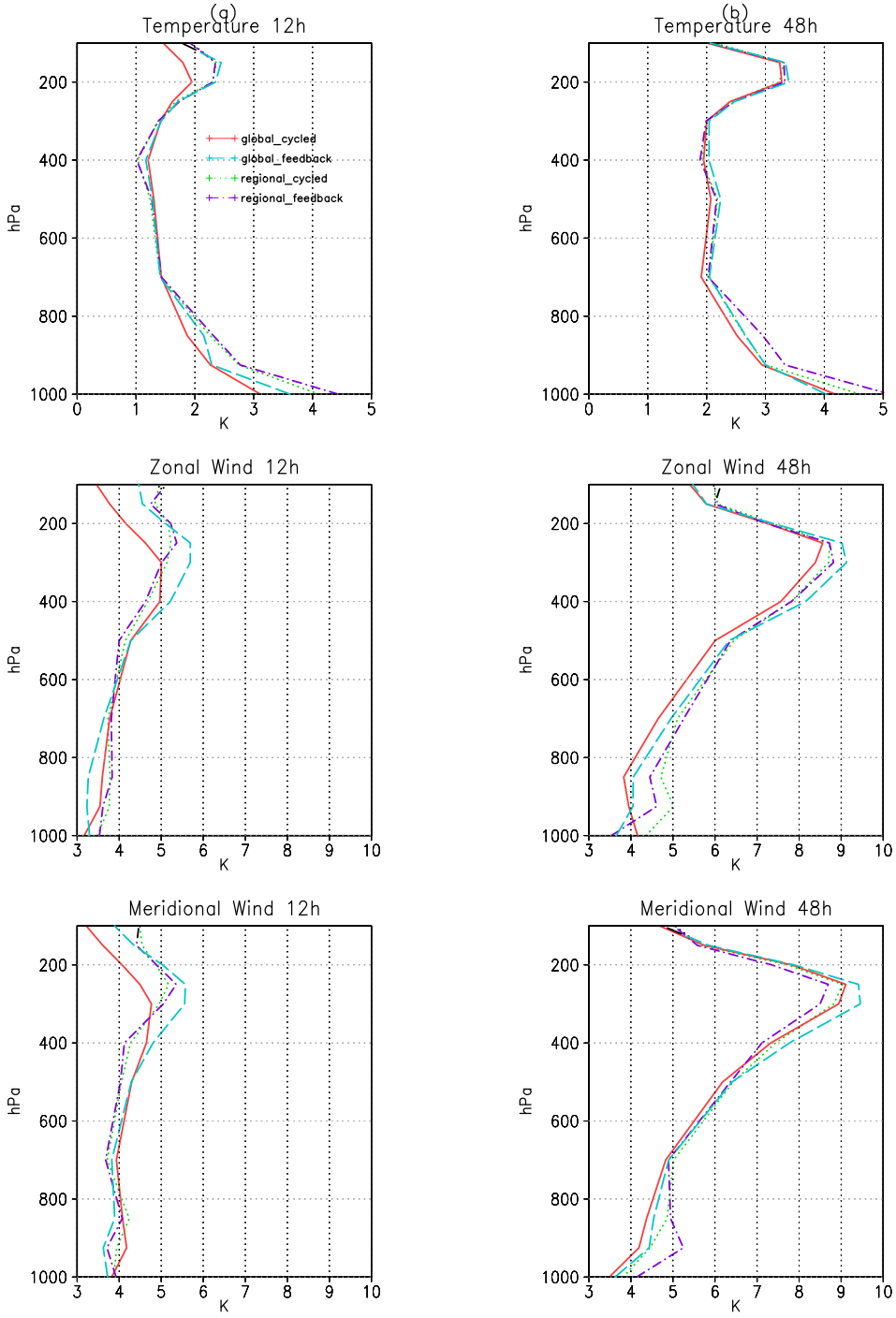

Appendix A

Regional Spectral Model

The RSM was developed at NCEP primarily for research purposes (Juang and Kanamitsu 1994; Juang et al. 1997). The Scripps Experimental Climate Prediction Center (ECPC) joined the efforts for the development and maintenance of the RSM in the early 1990s. Today it is one of the limited-area models used in the operational limited-area ensemble system at NCEP (Du et al. 2003, 2006). The RSM is also used at ECPC to provide fire danger forecasts, to study climate sensitivity, and to downscale reanalysis. Due to the flexibility of its design, the RSM can be easily implemented on a variety of computer architectures, a feature that makes the model appealing for use at universities and research institutes around the world.

The NCEP RSM is a perturbation model: the high resolution forecast it provides is the sum of the larger-scale flow component, as predicted by the NCEP GFS, and a high resolution perturbation component. To be precise, the NCEP RSM is not a true perturbation model because it does not solve the forecast equations directly for the perturbations. The tendencies are calculated as deviations of the full high resolution field from the global base field. Thus, it may be more correct to use the terminology *perturbation filtering model* (Kanamitsu 2000).

Unlike most other limited-area models, which are affected by the global fields only through the lateral boundary conditions, the RSM is affected by the global

fields throughout the entire limited area. Figure A.1 adapted from Juang et al. (1997) illustrates the nesting of the higher resolution field into the coarser grid of the global model (Juang and Hong 2001). The variable A represents a full high-resolution field of an arbitrary scalar model variable in the limited area, and A_g is the coarse resolution global field of the same variable. As shown in Figure A.1, in a typical limited-area model the effects of the coarse resolution global model are limited to a relaxation region near the border of the region. In contrast, the perturbation method considers the coarse global model over the whole limited area (Juang and Kanamitsu 1994). The perturbation field A', the dark shaded area in Figure A.1, is defined by

$$A' = A - A_g. \tag{A.1}$$

Features that cannot be resolved in the global spectral model, but can be resolved by the regional model are thus called perturbations. Nesting to the outer domain is done through relaxation of the perturbation term: the perturbation is zero at and outside of the regional domain boundaries and nonzero inside.

Since the base field is used in the entire regional domain, relaxation along the lateral boundary is sufficient to smooth the Gibbs effect of spectral representation. Additional blending between the regional and the global grids could achieve smoother lateral boundary fields, but may not be necessary to improve the forecast according to Juang and Kanamitsu (1994).

Integration of the RSM consists of the following steps:

1. The values of the global analysis $A_g(x, y)$ are obtained at each gridpoint within

the regional domain by an inverse spectral transformation from the spectral coefficients of the global field $A_g(m,n)$.

2. Equation A.1 directly calculates the perturbation $A'(x,y)$ within the limited area from the regional analysis, $A(x,y)$, and $A_g(x,y)$. $A'(x,y)$ is then converted into spectral space over the limited area to obtain the spectral coefficients $A'(k,l)$ for the perturbation. We note that the spectral transformation assumes that $A'(x,y)$ is zero at the boundary of the limited area.

3. The base field $A_g(m,n)$, the perturbation $A'(k,l)$, and their horizontal derivatives are then converted into grid space to obtain $A'(x,y)$, $A_g(x,y)$, $\frac{\partial A'}{\partial x}$, $\frac{\partial A'}{\partial y}$, $\frac{\partial A_g}{\partial x}$, and$\frac{\partial A_g}{\partial y}$. The vertical derivatives are approximated by the finite differences.

4. The full model tendency, $\frac{\partial A(x,y)}{\partial t}$, and the global tendency, $\frac{\partial A_g(x,y)}{\partial t}$, are then obtained and the perturbation tendency is calculated by

$$\frac{\partial A'(x,y)}{\partial t} = \frac{\partial A(x,y)}{\partial t} - \frac{\partial A_g(x,y)}{\partial t}. \tag{A.2}$$

5. The perturbation and global tendencies are transformed to spectral space. The spectral coefficients for the next time step are obtained from a semi-implicit time integration scheme. Time integration of the model is done separately for A' and A_g.

6. The integration of the model is carried on by returning to step 3.

Finally, we note that the NCEP RSM and GFS use the same physical parametrization packages, except for those used in very high resolution non-hydrostatic config-

urations of the RSM. Such high resolution configurations of the RSM are not considered in this research. The consistency of the physical parametrization packages minimizes the effects of the adjustment process that may occur due to differences between the global and regional model physics. This is an important potential advantage, since the presence of a strong adjustment process could degrade the quality of the estimates of the time dependent error statistics in the Kalman filter.

Figure A.1: One-dimensional representation of an arbitrary scalar variable in the regional model: (a) for a conventional limited area model; (b) for a perturbation model such as the NCEP RSM. The dotted curve represents the contribution from the global model, while the gray area represents the full high-resolution field.

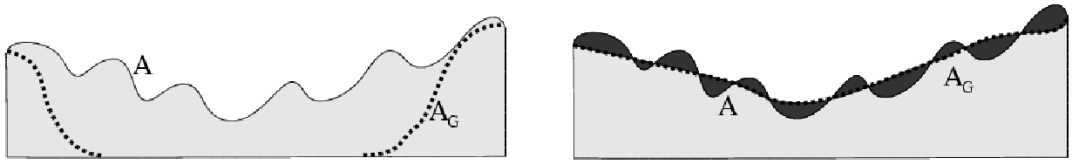

(a) conventional method (b) perturbation method

Appendix B

Significant test

The statistical significance of the difference between two experiments is tested by a two-sample t test for correlated data (Wilks 2006; Szunyogh et al. 2008). To perform the test, we first take the difference between the verified and the verifying data sets. (In our case the verifying data are radiosonde measurements at every 12 hours.) Then we take square of the difference and calculate the mean over all points in the verification domain. This way, we obtain two time series of the errors E_1^2 and E_2^2, one for each of the two experiments we compare. We define the Δ^i difference between the two time series, for each verification time by

$$\Delta^i = E_1^2(i) - E_2^2(i). \tag{B.1}$$

For the estimation of the efficient sample size, we also need to compute $\bar{\Delta}_- = (n-1)^{-1}\sum_{i=1}^{n-1}\Delta^i, \bar{\Delta}_+ = (n-1)^{-1}\sum_{i=2}^{n}\Delta^i, and \bar{\Delta} = n^{-1}\sum_{i=1}^{n}\Delta^i$. The total sample size in our case is $n = 30$. The effective sample size n' can be estimated using the approximation

$$n' \approx n(1-r_1)(1+r_1)^{-1}, \tag{B.2}$$

where the auto-correlation coefficient r_1 is

$$r_1 = \frac{\sum_{i=1}^{n-1}(\Delta^i - \bar{\Delta}_-)\sum_{i=2}^{n}(\Delta^{i+1} - \bar{\Delta}_-)}{[\sum_{i=1}^{n-1}(\Delta^i - \bar{\Delta}_-)^2 \sum_{i=2}^{n}(\Delta^i - \bar{\Delta}_+)^2]^{1/2}}. \tag{B.3}$$

This approach to compute the efficient sample size is based on the assumption that the random variable $\Delta^i, i = 1, ..., n$, describes a first-order autoregressive process.

If there was no auto-correlation between Δ^i at the different verification times, the effective sample size n' would be equal to the sample size n , but with increasing r_1, the effective sample n' decreases.

The t-test is based as the assumption that the test statistic

$$z = \frac{\bar{\Delta}}{(s_\Delta^2/n')^{1/2}} z = \frac{\bar{\Delta}}{(sd/n')^{1/2}} \tag{B.4}$$

, where s_Δ is the sample variance of Δ^i, a normally distributed random variable. is normally distributed. We compare this value to the probabilities of the standardized normal distribution and determine likelihood of the difference.

We claim, that the difference between errors in the two experiments is significant at level x, if the probability of the null hypothesis, that $\bar{\Delta}$ is different from zero only due to statistical fluctuations, is less then $100 - x\%$. For example, we can say that difference between 12-hr forecast of the regional cycled and the feedback strategy in Table B.1 is significantly different at 99% level if the values of the z are not bigger then -2.57 (Table B.1 in Wilks (2006)).

Table B.1: z values for the difference of the regional cycled and the regional real data feedback experiment for 12-hr forecast time.

Level	925	850	700	500	400	300	250	150	70	50
Temperature	-0.17	-0.15	-0.12	0.14	-0.09	-0.13	0.12	-0.11	0.09	-0.09
Zonal wind	-0.13	0.11	0.18	0.15	0.09	-0.11	-0.13	0.13	-0.2	0.13
Meridional wind	0.15	-0.11	0.14	0.1	0.08	0.07	0.12	0.23	0.17	0.18

Table B.2: z values for the difference of the regional cycled and the regional feedback real data experiment for 48-hr forecast time.

Level	925	850	700	500	400	300	250	150	70	50
Temperature	-0.15	0.19	0.11	0.14	-0.12	-0.16	-0.13	-0.13	0.03	0.08
Zonal wind	0.12	-0.11	0.14	0.13	0.14	0.12	-0.14	0.11	0.07	0.15
Meridional wind	-0.18	0.14	-0.11	0.13	0.09	0.07	0.08	-0.07	-0.12	0.11

Table B.3: z values for the difference of the global cycled and the global feedback real data experiment for 12-hr forecast time.

Level	925	850	700	500	400	300	250	150	70	50
Temperature	-0.18	-0.13	-0.17	-0.13	-0.10	-0.11	-0.09	-0.09	-0.14	-0.10
Zonal wind	0.12	-0.18	-0.13	-0.16	-0.12	-0.10	-0.11	-0.14	-0.14	-0.13
Meridional wind	-0.12	-0.13	-0.16	-0.14	-0.12	-0.09	-0.11	-0.13	-0.17	-0.14

Table B.4: z values for the difference of the global cycled and the global feedback real data experiment for 48-hr forecast time.

Level	925	850	700	500	400	300	250	150	70	50
Temperature	-0.17	-0.12	-0.12	-0.16	-0.12	-0.13	-0.14	-0.10	0.12	-0.11
Zonal wind	-0.11	-0.15	-0.14	-0.14	-0.15	-0.15	-0.08	0.08	-0.10	0.10
Meridional wind	-0.16	-0.15	-0.09	-0.08	-0.09	-0.08	-0.07	-0.07	-0.11	0.10

Bibliography

Bishop, C. H., B. J. Etherton, and S. J. Majumdar, 2001: Adaptive sampling with the ensemble transform Kalman filter. Part I: Theoretical aspects. *Mon. Wea. Rev.*, **129**, 420–436.

Du, J., G. DiMego, S. Tracton, and B. Zhou, 2003: NCEP short-range ensemble forecasting (SREF) system: multi-IC, multi-model and multi-physics approach. Tech. Rep. 33, 5.09-5.10 pp. Electronic publ.

Du, J., J. McQueen, G. DiMego, Z. Toth, D. Jovic, B. Zhou, and H. Chuang, 2006: New dimension of NCEP short-range ensemble forecasting (SREF) system: Inclusion of WRF members preprint. Tech. rep. Preprint.

Fertig, E. J., et al., 2008: Observation bias correction with an ensemble Kalman filter. *Tellus*.

Harris, L. M. and D. R. Durran, 2010: An idealized comparison of one-way and two-way grid nesting. *Mon. Wea. Rev.*, **138**, 2174–2187.

Huang, X. Y., et al., 2009: Four-dimensional variational data assimilation for WRF: Formulation and preliminary results. *Mon. Wea. Rev.*, **137**, 299–314.

Hunt, B., E. Kostelich, and I. Sunyogh, 2007: Efficient data assimilation for spatiotemporal chaos: a local ensemble transform kalman filter. *Physica D*, **236**, 112–126.

Hunt, B. R., et al., 2004: Four-dimensional ensemble Kalman filtering. *Tellus*, **56A**, 273–277.

Juang, H. M. H., 1992: A spectral fully compressible nonhydrostatic mesoscale model in hydrostatic sigma coordinates: Formulation and preliminary results. *Meteorol. Atmos. Phys.*, **50 (1)**, 75–88.

Juang, H. M. H. and S. Y. Hong, 2001: Sensitivity of the NCEP Regional Spectral Model to domain size and nesting strategy. *Mon. Wea. Rev.*, **129 (10)**, 2904–2922.

Juang, H. M. H., S. Y. Hong, and M. Kanamitsu, 1997: The NCEP Regional Spectral Model: An update. *Bull. Amer. Meteor. Soc.*, **78 (10)**, 2125–2143.

Juang, H. M. H. and M. Kanamitsu, 1994: The NMC nested Regional Spectral Model. *Mon. Wea. Rev.*, **122 (1)**, 3–26.

Kalnay, E., 2002: *Atmospheric modeling, data assimilation, and predictability*. Cambridge University Press, Cambridge.

Kanamitsu, M., 2000: RSM short course GSM/RSM basics. *The Second International RSM Conference, MHPCC, Mauii, Hi, July 17-21.*

Lynch, P. and P. M. Huang, 1992: The emergence of numerical weather prediction: Richardsons dream. *Mon. Wea. Rev.*, **120**, 1019–1034.

Ott, E., et al., 2004: A local ensemble Kalman filter for atmospheric data assimilation. *Tellus*, **56A (5)**, 415–428.

Sela, J. G., 1980: Spectral modeling at the National Meteorological Center. *Mon. Wea. Rev.*, **108**, 1279–1292.

Szunyogh, I., E. J. Kostelich, G. Gyarmati, E. Kalnay, B. R. Hunt, E. Ott, E. Satterfield, and J. A. Yorke, 2008: A local ensemble transform Kalman filter data assimilation system for the NCEP global model. *Tellus*, **60A**, 113–130.

Szunyogh, I., Z. Toth, S. J. M. R. E. Morss, B. J. Etherton, and S. H. Bishop, 2000: The effect of targeted dropsond observations during the 1999 winter storm reconnaissance program. *Mon. Wea. Rev.*, **128**, 3520–3537.

Tippett, M. K., J. L. Anderson, C. H. Bishop, T. M. Hamill, and J. S. Whitaker, 2003: Ensemble square-root filters. *Mon. Wea. Rev.*, **131**, 14851490.

Torn, R. D., G. J. Hakim, and C. Snyder, 2006: Boundary conditions fro limited-area ensemble Kalman filters. *Mon. Wea. Rev.*, **134**, 2490–2502.

Warner, T. T., R. A. Peterson, and R. E. Treadon, 1997: A tutorial on lateral boundary conditions as a basic and potentially serious limitation to regional numerical weather prediction. *Bulletin of the American Meteorological Society*, **78 (11)**, 2599–2617.

Wilks, D. S., 2006: *Statistical Methods in the Atmospheric Sciences*. Elsevier.

Zhang, F., Z. Meng, and A. Aksoy, 2006: Tests of an ensemble Kalman filter for mezoscale and regional-scale data assimilation. part I: Perfect model experiments. *Mon. Wea. Rev.*, **134**, 722–736.